

U.S. DEPARTMENT OF COMMERCE  
National Technical Information Service

AD-A025 223

THE MAXIMUM LIKELIHOOD METHOD APPLICATIONS TO  
DAASM STUDIES

BOSTON COLLEGE

PREPARED FOR  
AIR FORCE CAMBRIDGE RESEARCH LABORATORIES

30 JUNE 1975

# THE MAXIMUM LIKELIHOOD METHOD APPLICATIONS TO DAASM STUDIES

Rajan Varad

William C. McCormish

Space Data Analysis Laboratory

Boston College

Chestnut Hill, Massachusetts 02167

30 June 1975

FINAL REPORT FOR PERIOD 1 NOVEMBER 1974 — 30 JUNE 1975

APPROVED FOR PUBLIC RELEASE

DISTRIBUTION UNLIMITED

AIR FORCE CAMBRIDGE RESEARCH LABORATORIES  
AIR FORCE SYSTEMS COMMAND  
UNITED STATES AIR FORCE  
MENLO PARK, MASSACHUSETTS 01731

Qualified requestors may obtain additional copies from the Defense Documentation Center. All others should apply to the National Technical Information Service.

REPORT DOCUMENTATION PAGE		READ INSTRUCTIONS BEFORE COMPLETING FORM
1. REPORT NUMBER AFCRL-TR-75-0551	2. GOVT ACCESSION NO.	3. RECIPIENT'S CATALOG NUMBER
4. TITLE (and Subtitle)  THE MAXIMUM LIKELIHOOD METHOD - APPLICATIONS TO DAASM STUDIES		5. TYPE OF REPORT & PERIOD COVERED 1 NOV 75 /- 30 JUN 75 Scientific-Final
7. AUTHOR(s)  Rajan Varad William C. McComish		6. PERFORMING ORG. REPORT NUMBER B.C. 76-01
9. PERFORMING ORGANIZATION NAME AND ADDRESS Space Data Analysis Laboratory Boston College Chestnut Hill, Ma 02167		10. PROGRAM ELEMENT, PROJECT, TASK AREA & WORK UNIT NUMBERS 7663-01-01 61102F
11. CONTROLLING OFFICE NAME AND ADDRESS Air Force Cambridge Research Laboratories Hanscom AFB, Massachusetts 01731 Contract Monitor: Gary S. Sales		12. REPORT DATE 30 June 1975
14. MONITORING AGENCY NAME & ADDRESS (if different from Controlling Office)		13. NUMBER OF PAGES 62
15. SECURITY CLASS. (of this report)  Unclassified		
15a. DECLASSIFICATION/DOWNGRADING SCHEDULE		
16. DISTRIBUTION STATEMENT (of this Report)  Approved for Public Release; Distribution Unlimited		
17. DISTRIBUTION STATEMENT (of the abstract entered in Block 20, if different from Report)		
18. SUPPLEMENTARY NOTES		
19. KEY WORDS (Continue on reverse side if necessary and identify by block number)  Maximum Likelihood method, Frequency wavenumber spectra, DAASM studies, Simulated Models, Ionospheric Research		
20. ABSTRACT (Continue on reverse side if necessary and identify by block number)  The MLM has been applied to simulated models of signals and noise to ascertain Doppler and angular information. The models closely correspond to HF signals propagating through the ionosphere. Relevant mathematical derivations and properties are presented. Examples of the technique as applied to actual data are also presented.		

TABLE OF CONTENTS

<u>Section</u>		<u>Page</u>
	LIST OF ILLUSTRATIONS	iv
	LIST OF TABLES	v
	PREFACE	vi
1.	INTRODUCTION	1
2.	DESCRIPTION OF THE EXPERIMENT	3
	2.1 Overall Project	3
	2.2 Estimation of Cross Spectra	5
	2.3 Power Spectra	5
	2.4 Coherence Spectra	7
	2.5 Frequency Wavenumber	8
3.	MATHEMATICAL DERIVATIONS AND PROPERTIES OF THE MLM ESTIMATOR	12
	3.1 Minimum Variance Unbiased Estimate	12
	3.2 Properties of the Minimum Variance Estimate	13
	3.3 Maximum Likelihood Estimate (MLM)	14
	3.4 Estimation of MLM FWPD Spectra	16
	3.5 A Relevant Theorem and Additional Properties	19
	3.6 Random Noise and Two Plane Waves	21
	3.7 Computational Procedure	24
4.	RESULTS	
	4.1 Simulated Models of Signals and Random Noise	26
	4.2 Parameter Variations and Digicoder Displays	26
5.	CONCLUSIONS	28
	5.1 Incoherent Sources	28
	5.2 Coherent Sources	29
	TABLES AND ILLUSTRATIONS	31
	REFERENCES	55

Preceding page blank

LIST OF ILLUSTRATIONS

<u>Figure</u>		<u>Page</u>
1	Effect of Smoothing	33
2	Doppler Proximity, 7 Point Smoothing	35
3	Doppler Proximity, 15 Point Smoothing	37
4	Angular Proximity, Narrow Doppler-spacing	39
5	Angular Proximity, Wide Doppler-spacing	41
6	6-Antenna Configurations, Narrow Doppler-spacing	43
7	6-Antenna Configurations, Wide Doppler-spacing	45
8	6-Antenna Configurations, Coherent Sources	47
9	12- and 11-Antenna Configurations, Incoherent Sources	49
10	12- and 11-Antenna Configuration, Coherent Sources	51
11	DAASM Data A/C Flight 196-4 Power Spectra, Coherence Spectra and DAASM Maps	53

LIST OF TABLES

<u>Table</u>		<u>Page</u>
1	Legend for Fig. 1 (Effect of Smoothing)	32
2	Legend for Fig. 2 (Doppler Proximity)	34
3	Legend for Fig. 3 (Doppler Proximity)	36
4	Legend for Fig. 4 (Angular Proximity, Incoherent Sources)	38
5	Legend for Fig. 5 (Angular Proximity, Incoherent Sources)	40
6	Legend for Fig. 6 (Antenna Configurations)	42
7	Legend for Fig. 7 (Antenna Configurations)	44
8	Legend for Fig. 8 (Coherent Sources)	46
9	Legend for Fig. 9 (Antenna Configuration)	48
10	Legend for Fig. 10 (Coherent Sources)	50
11	For Data Sample: Flight 4-196, 15 July 1974, UT 2100	52
12	Digicoder Integers ↔ Coherence Values	54

## PREFACE

Dr. Gary S. Sales, in addition to being the Contract Monitor, has been the guiding force behind this project and the authors are indebted for his encouragement.

The initial computer programming contributions to this study were provided by Mr. Robert F. Boudreau, Boston College and the authors are very grateful for his assistance.

Dr. Wolfgang Pfister who is the originator of the DAASM concept and the experiment has contributed substantially to this study with his timely and penetrating suggestions in his capacity as a consultant on the project.

Many thanks are due Miss Mary Kelly of Boston College, for her excellent job in typing a difficult manuscript.

## 1. INTRODUCTION

This report discusses the theory, applications and performance of various stages of analysis and data processing involved in the DAASM (Doppler arrival angle spectral measurements) Project. The analysis can be divided into three stages, namely:

- 1) Power spectral estimation
- 2) Coherence analysis
- 3) Doppler frequency - angle of arrival estimation (DAASM maps)

The power spectral, coherence and DAASM maps are presented in the form of digicodec printouts. The printouts display integers 0 to 15 in a gradation of increasing intensity.

Much of the analysis pertaining to the power spectra and coherence has been dealt with in detail in previous AFCRL reports. Only brief and necessary material are discussed here. The main portion of this report deals with the adaptive data processing aspect of the DAASM maps. Several test functions have been devised to simulate sources at different Doppler frequencies and different arrival angles and with various levels of isotropic white noise. The simulation is performed on linear arrays of six and twelve antenna elements corresponding to most often used configurations for measuring and gathering real data.

The work described here has evolved out of a need to extract the Doppler frequencies and the direction of arrival of high frequency radio signals propagating through the ionosphere and received on a linear array of antennas. The concept of a homogeneous random electromagnetic field in the sense of Yaglom [5] propagating across an array of sensors has been employed. If the random field can be considered as a wide-sense stationary process it is possible to apply a multi-dimensional Fourier transformation and obtain the so-called Frequency - Wavenumber Power Density Spectrum (FWPD). The frequency dimension resolves the Doppler or temporal components while the wavenumber dimension yields the direction of arrival or the spatial components of the array data.

The frequency-wavenumber approach has been developed and widely used in the processing of seismic signals by Capon et al. [1]. All spectral analysis

techniques utilize some or other form of data windows either in the original untransformed domain or in the transformed domain. Data windows are necessary to reduce the statistical variability of the spectral estimate and also to suppress sidelobe leakage. As a consequence the choice of data windows has to compromise between conflicting requirements of spectral resolution and statistical stability. Besides, the data windows in usual spectral analysis are of a fixed nature in that they do not depend on the data or noise characteristics. The data window is a taper function applied to the estimated correlation function and the product is transformed to get the spectrum. Consequently, the estimated spectrum is smeared by the convolution of the window function and the true spectrum. The selection of a suitable data window becomes very critical when only limited data are available or cannot be processed because of stationarity considerations and adequate resolution has to be maintained.

Spectral techniques which are data-adaptive and offer higher resolution than usual methods have been increasingly used in seismology as mentioned above. The maximum likelihood method of estimation of the frequency-wavenumber spectrum which is employed in this study belongs to the data-adaptive high resolution class of spectral estimators. The method as applied to multi-channel streams of complex valued data points from a two-dimensional array of antennas in the Doppler-arrival-angle-spectral measurements (DAASM) experiment has been discussed and derived in detail in an AFTRL report by (Pfister, Sales and Vrad) [2]. There, the method is rendered data-adaptive in both the temporal as well as the spatial domains. But it suffers from the disadvantage that the core and time requirements for computer processing become unrealistic as the number of antennas and time data points are increased. It is probably feasible on such giant parallel computer systems as the Iliac IV.

Moreover, the improvement observed in the frequency dimension does not justify the additional complexity contrasted with simpler and much faster methods utilizing the Fast Fourier Transform. Therefore, the technique as employed here is adaptive only in the spatial domain, since it is conceivable that the number of available spatial data points is normally far less than the number of time domain data points.

## 2. DESCRIPTION OF THE EXPERIMENT

### 2.1 Overall Project

The DAASM system consists of a twenty-element array, eleven of which are to form a minimum redundancy (MR) configuration as described by Richards [3] in a previous AFCRL report. This means that by proper selection of antennas it is possible to obtain spacings equal to successive multiples of an available minimum spacing. It can also be used in quasi-minimum redundancy configurations where the available spacings are near successive multiples. The advantage of the MR array is that it is equivalent to a large filled array with the same aperture and the same basic spacing. The signals incident on the antennas are sampled in time and recorded in the form of complex-valued digital data after proper IF conversion of the carrier frequency. The pulses at chosen carrier frequencies originate either from a flying aircraft or from a ground-based transmitter.

The object of subsequent processing of the recorded data is to extract the spatial and temporal characteristics of the signals. To describe these characteristics it is necessary to introduce the concept of a frequency-wavenumber power density (FWPD) spectrum. In the case of acoustic and seismic signals, wavenumber is a quantity which describes waves in terms of their velocities, that is, speed and direction, are both variable. But for electromagnetic waves wavenumber is only dependent on direction since the speed is constant in a given homogeneous medium.

If the time samples are understood to constitute one dimension and the spatial samples to be the second dimension then the two-dimensional Fourier transform yields the frequency wavenumber power density (FWPD) spectrum.

Thus, if  $A_j(w)$  and  $A_m(w)$  denote the discrete complex Fourier spectrum at radial frequency  $w$  at antennas  $j$  and  $m$  then the cross spectrum between the antennas  $j$  and  $m$  at frequency  $w$

$$\hat{S}_{jm}(w) = A_j(w) \cdot A_m^*(w) .$$

In general, a smoothed version of cross-spectral estimates  $S_{jm}(w)$  is used. The estimated FWPD spectrum is defined by

$$P(w, \vec{k}) = \sum_{j=1}^N \sum_{m=1}^N w_j w_m \hat{S}_{jm}(w) \cdot \exp \left\{ i \vec{k} \cdot (r_j - r_m) \right\} \quad (2.1.1)$$

where  $N$  is the total number of antennas,  $r_n$ 's are the vector distances from some arbitrary origin,  $\vec{k}$  is the wavenumber vector and the  $w_j$ 's are suitable weights imposed on the  $j$ th antenna.

In a previous report [4], different methods of spectral analysis to extract frequency, phase and coherence information were described in detail. It was found that the frequency-averaging technique provided a very efficient and reliable means of cross-spectral estimation. Although it is true that the maximum likelihood method of spectral analysis provides an optimal estimation of the spectrum, it proves to be very costly in terms of computer time and memory requirements and the improvement obtained thereof is not substantial. As the number of antennas is increased, the analysis soon becomes impractical. Therefore, only the frequency-averaging technique of estimating the cross-spectra is used in all of the data involved here. Once the cross-spectra have been estimated, the spatial component of the FWPD spectrum can be estimated by various methods. In the subsequent analysis three methods of estimation of the angle of arrival have been implemented. The three methods can be delineated in terms of the choice of the weights  $w_j$  and are: (1). The Fast Frequency Wavenumber Analysis or the Conventional Analysis, which is most useful for an initial diagnostic scan in the frequency-wavenumber ( $f$ - $k$ ) space. Wavenumber sidelobe characteristics can be varied by proper choice of weights for the different cross-spectral terms. But resolution is poorer than methods 2 and 3. (2). The minimum redundancy version which is only applicable to the data from a strict minimum redundancy configuration of the antennas. Sidelobes are better but the technique suffers from grating lobes having amplitudes equal to the mainlobe whenever the basic antenna spacing exceeds half the operating wavelength. (3). An adaptive method using the maximum likelihood principle offers high resolution in spatial characteristics and is applicable to any arbitrary antenna configuration. Unlike the other two methods, this method assigns adaptive weights to the different cross-spectral terms depending on the look-angle and the spatial characteristics of interference and noise.

Each of these three approaches will be briefly outlined here. The common part of the analysis and computation to all three methods is to obtain suitable cross-spectral estimates between any given pair of antennas.

## 2.2 Estimation of Cross Spectra

The recorded data consists of two sets of 256 equally spaced complex valued time samples from each antenna output. Although the entire 256 samples could be used for further processing, it was decided to treat only the middle 128 samples in each set for reasons of economy. Thus, the truncated sets consisting of 128 samples in each subcase are immediately transformed into the frequency domain via a Fast Fourier Transform. The resulting 128 complex-valued discrete Fourier spectra stretches across a basic Doppler frequency range of 8 Hz. The two sets of time samples are displaced from each other by an amount  $\beta = \frac{6}{25}$  of the sampling period. Therefore, it is possible to either align or interlace the resulting two sets of Fourier spectra. If the Fourier spectra are aligned the signal-to-ratio can be improved but the basic Doppler frequency range is still 8 Hz. On the other hand, if the two sets are interlaced the frequency range can be doubled to 16 Hz without any improvement in the signal-to-noise ratio.

In the case of signals transmitted by an aircraft, the basic range of 8 Hz is sufficient. But ground backscatter signals often occupy a band wider than 8 Hz, in which case interlacing proves to be very useful. In any case, the combined or interlaced Fourier spectra from the starting point for further data processing.

Three types of output have been designed. These consist of (1) power spectra, (2) coherence spectra, and (3) maps of Doppler frequency\*vs\*arrival angle called DAASM maps.

## 2.3 Power Spectra

Power spectra are calculated for each antenna by taking the product of each Fourier spectral line with its own complex conjugate. Of course, the Fourier

spectra are normalized in each channel so that the total power in each channel equals unity. That is, if  $g'_{mA}$  represents the unnormalized  $m^{\text{th}}$  frequency line, then the normalized Fourier spectrum is simply

$$g_{mA} = g'_{mA} / \sqrt{\sum_{m=1}^N g'_{mA} g'^*_{mA}} \quad (2.3.1)$$

The power spectra are smoothed by the frequency-averaging technique [2] over 7 frequencies concurrently with the operation of evaluating the product of the Fourier spectra. This feature enables the cross-spectra to be estimated in an identical way merely by inserting the Fourier spectra of the appropriate pair of antennas. The power spectra and the cross-spectra are different only in a matter of identification of antenna elements.

The power spectra thus obtained are plotted on a standard digicoder format of logarithmically scaled numbers ranging from 1 to 15 which corresponds to a linear scale from 0 to 100. The exact equation defining the scales is

$$\begin{aligned} DI &= 2 + 7 \log_{10} P_{\text{lin}} & 1 < P_{\text{lin}} < 100 \\ &= 2 \times P_{\text{lin}} & P_{\text{lin}} < 1 \end{aligned}$$

where DI is the digicoder output integer and  $P_{\text{lin}}$  is the value of the power designed to have a maximum of 100.

The details of the Preface and Data format are given in [4]. The power spectral digicoder printouts/outputs provide the basis for selection of data segments suitable for more complex and time consuming analysis. A representative segment of data is presented in Figure 11. The data as usual consists of sub-cases where each subcase has four different height gates and two carrier frequencies. Therefore, for the six antenna configuration there will be 48 channels of power spectra for each subcase. A preface line separates each height gate and the subcases themselves are separated from each other by 6 preface lines.

## 2.4 Coherence Spectra

Coherence spectra between the  $m^{\text{th}}$  and  $n^{\text{th}}$  channels is defined by the equation

$$[\text{coh}(f)_{mn}] = \frac{|\hat{S}_{mn}(f)|}{\sqrt{\hat{S}_{mm}(f) \hat{S}_{nn}(f)}} \quad (f = \frac{w}{2\pi}) \quad (2.4.1)$$

where  $\hat{S}_{mn}$  is the smoothed cross spectrum at frequency  $f$  between  $m^{\text{th}}$  and  $n^{\text{th}}$  channels and  $S_{mm}(f)$  would be the self power spectrum of the  $m^{\text{th}}$  channel and so on. It is clear that the coherence is a number which lies between 0 and 1. This linear range is converted to an arc hyperbolic tangent scale and multiplied by a suitable scale factor to provide the digicoder output numbers.

Table 12 shows the relationship between coherence and digicoder output numbers. The coherence spectra are plotted for each available distance between the various pairs of antennas in order of increasing distance. Since the coherence is only available at specified distances the plots are backfilled at intermediate distances. It was found the raw coherence thus plotted appeared sometimes to be a discontinuous function of distance instead of monotonically decreasing function. Therefore, three successive subcases have been averaged for each distance at each Doppler frequency to provide a much smoother picture and thus the statistical confidence limits which depend on any given sample size are improved (see Fig. 11).

The coherence is a good measure of the spatial extent of the frequency-wavenumber spectrum, when the number of sensors is small. Looking from another point of view, the coherence can be interpreted as a measure of the relative amounts of propagating and non-propagating noise. However, direct evaluation of the FWPD is a superior approach and contains all the information.

The coherence spectra are primarily useful to determine the maximum meaningful aperture in terms of operating wavelength for the type of signals involved. A smooth ionosphere (certain ionospheric modes) produces signals with high spatial stationarity. In such a case the coherence does not decay rapidly with increasing distance. On the other hand, a turbulent ionosphere displays high coherence over relatively smaller apertures. Digicoder plots of the coherence spectra are presented for various selected data segments elsewhere [4].

## 2.5 Frequency-Wavenumber Spectra

DAASM maps consist of digicoder plots of frequency against wavenumber which in turn is easily related to the angle of arrival.

A particularly efficient algorithm to calculate the f-k spectra is possible if the weights in Equation (2.1.1) are chosen to correspond to a triangular taper function and will be referred to as Fast Frequency Wavenumber analysis or the generalized Bartlett estimate. In such a case, the individual cross-spectral terms need not be separately calculated.

The separate Fourier spectra from each antenna output can be used directly and frequency smoothing can be applied in the final step. The details of the algorithm are as follows:

Let  $|A_j(w)| \exp i\phi_j(w)$  represent the Fourier spectral line at frequency  $w$  from the  $j$ th antenna. Then the cross-spectrum between the  $j$ th and  $m$ th antennas is

$$S_{jm}(w) = |A_j(w)| |A_m(w)| \exp i(\phi_j - \phi_m) \quad (2.5.1)$$

and the f-k spectrum

$$P(w, \vec{k}) = \sum_{j=1}^N \sum_{m=1}^N S_{jm}(w) \exp \left\{ -i\vec{k} \cdot (\hat{r}_j - \hat{r}_m) \right\} \quad (2.5.2)$$

where  $\vec{k}$  is the wavenumber and where  $w = 2\pi f$ .

Equation (2.5.2) can be written alternately as

$$\begin{aligned} P(w, \vec{k}) &= \sum_{j=1}^N |A_j(w)| \exp i \left\{ \phi_j(w) - \vec{k} \cdot \hat{r}_j \right\} \\ &\times \sum_{m=1}^N |A_m(w)| \exp -i \left\{ \phi_m(w) - \vec{k} \cdot \hat{r}_m \right\} \end{aligned}$$

The subscripts  $j$  and  $m$  can be replaced by a single subscript  $n$  and the double summation can be replaced by a single summation. Thus,

$$P(w, \vec{k}) = \left| \sum_{n=1}^N A_n(w) \exp i \left\{ \phi_n(w) - \vec{k} \cdot \hat{r}_n \right\} \right|^2 \quad (2.5.3)$$

Equation (2.5.3) can be computed much faster than equation (2.5.2).

$P(w, \vec{k})$  is calculated at as many points as desired in  $\vec{k}$ , say with increments  $\Delta \vec{k}$ . Each successive point in  $\vec{k}$  can be computed from the previously computed point by simple complex multiplication because  $\exp i (\vec{k} + \Delta \vec{k}) = \exp i \vec{k} \cdot \exp i \Delta \vec{k}$ . This step is common to all three approaches of f-k spectral calculations and saves considerable computer memory and time.

Since frequency smoothing is independent of the operations on  $\vec{k}$  a set of weights  $W(w)$  is calculated using  $P(w, \vec{o})$  for each  $w$  and each  $P(w, \vec{k})$  is multiplied by the appropriate  $W(w)$  to yield  $\hat{P}(w, \vec{k})$ , the frequency smoothed estimate. The relation between the wavenumber  $\vec{k}$  and the direction of arrival  $\theta$  for the case of a linear array is given by

$$\vec{k} = |k| = \frac{2\pi f \cos\theta}{c}$$

where  $k$  is now a scalar,  $f$  the operating carrier frequency and  $c$  the velocity of light.

The minimum redundancy version can be treated as a special case of the general equation for the f-k spectra given by Equation (2.1.1). It is assumed, of course, that a certain number of consecutive multiples of the basic antenna spacing are available by suitably placing the different antennas. Distances beyond the largest consecutive multiple are regarded to have zero weight, i.e., their contribution to the f-k spectra is nil. The non-zero weights decrease as a cosine squared function with distance. In addition, the self-spectral term is assigned a weight of 0.5, so that the expression for the f-k spectrum can be written as

$$P(w, \vec{k}) = 1/2 S_0 + \sum_{\ell=1}^L W_\ell S_\ell \exp i (k \cdot d_\ell)$$

where  $S_0$  corresponds to the self term and  $S_\ell$  is the cross-spectral term corresponding to the pair of antennas separated by a distance  $d_\ell$ ,  $L$  is the largest successive multiple of the basic spacing and  $W_\ell$  is the weight given by the cosine-squared function. It is well known that the cosine-squared weights result in good sidelobe suppression. It can be shown that for six antennas only ten consecutive multiples are possible and for eleven antennas the corresponding number is 45. A similar configuration for more than eleven antennas is not known at present. Each distance occurs only once and hence the name 'minimum redundancy' for the array. Only those cross-spectral terms corresponding to the multiples of the basic spacing need be calculated. Thus, for eleven antennas 45 of 66 possible terms are necessary resulting in almost a 30% reduction in calculations. More than that, in a sense, the weights are almost optimal for the configuration and there is excellent sidelobe suppression. The carrier frequency can be chosen such that the basic spacing is a half-wave length or smaller, thus avoiding grating lobes.

The maximum likelihood FWPD spectrum is derived from sets of filters which are data-adaptive and optimal. The filters are optimal in the sense that a unit plane wave propagating across the array of sensors arriving from a particular direction is passed undistorted while signals and noise from other directions are minimized in a mean square error sense. When the noise distribution is assumed to be multi-dimensional Gaussian, the results are identical with the maximum likelihood estimate of the signal calculated from the likelihood functions of signal plus noise.

This method of f-k spectral estimation employs an adaptive scheme to generate the set of weights in the filter given by Equation (2.1.1). Instead of using a fixed set of weights for all  $k$  the adaptive scheme allows for the set of weights to be varied depending on the particular  $k$  as well as signal, interference and noise characteristics. In other words, the set of weights is dictated by the data sample available, subject to the constraints that a unit plane wave

signal travelling with a given wavenumber  $k = k_0$  (arriving from the direction towards which the antenna beam is pointed), is passed undisturbed through the spatial filter but everything else for which  $k \neq k_0$  (arriving from other directions) is rejected in an optimal manner. Thus, the true spectrum is reproduced with high resolution and not smeared, which is the result of convolution between the true spectrum and the particular spectral window chosen. This choice of constraints results in a convenient mathematical formulation. It is only necessary to calculate the inverse of the matrix of cross-spectral terms for each Doppler frequency of interest, in order to furnish the optimal set of weights automatically adapted to each  $k$  for a given data sample.

### 3. MATHEMATICAL DERIVATIONS AND PROPERTIES OF THE MLM ESTIMATOR

#### 3.1 Minimum-Variance Unbiased Estimate

Consider the set of measurements

$$\vec{z} = \vec{Hx} + \vec{v}$$

where  $\vec{z}$  is the measurement vector,  $\vec{x}$  is a constant signal vector.  $\vec{v}$  is the additive random noise vector and  $H$  is the signal model matrix. If  $A$  is the filter set that minimizes the mean square error between the signal vector  $\vec{x}$  and the estimated vector  $\hat{\vec{x}}$  then

$$\hat{\vec{x}} = A^H \vec{z}$$

where the superscript  $H$  is the conjugate transpose. If  $A$  is so chosen that  $\vec{v}$  is rejected by the filter but  $\vec{Hx}$  is passed undistorted then

$$\vec{Hx} = HA^H \vec{z} = HA^H \vec{Hx}$$

or  $1 = HA^H$  and by symmetry  $AH^H = 1$  which is the constraint expressed mathematically.

Now the variance of  $\hat{\vec{x}}$  can be written as

$$\sigma^2 = A^H R A$$

where  $R$  is the covariance matrix of the noise process.

If  $\sigma^2$  is minimized under the constraint

$$H^H A = 1$$

Then a quadratic cost function  $J$  can be written as

$$J = A^H R A + \lambda (H^H A - 1)$$

$J$  is minimized when  $\frac{\partial J}{\partial A} = 0$

or

$$A^H R + \lambda H^H = 0$$

$$A^H = -\lambda H^H R^{-1}$$

$$A^H H = -\lambda H^H R^{-1} H$$

$$-\lambda = +\frac{A^H H}{H^H R^{-1} H} = +\frac{1}{H^H R^{-1} H}$$

$$A^H = \frac{H^H R^{-1}}{H^H R^{-1} H}$$

$$\hat{x} = A^H z = (H^H R^{-1} H)^{-1} H^H R^{-1} z \quad (3.1.1)$$

### 3.2 Properties of the Minimum Variance Estimator

From Equation (3.1.1)

$$\hat{x} = (H^H R^{-1} H)^{-1} H^H R^{-1} z$$

$$\hat{x}_k = (H_k^H R_{kk}^{-1} H_k)^{-1} H_k^H R_{kk}^{-1} \hat{z}_k$$

where  $k$  = dimension of the measurement vector premultiplying the equation

$$z_k = H_k \hat{x} + \hat{v}_k$$

by  $(H_k^H R_{kk}^{-1} H_k)^{-1} H_k^H R_{kk}^{-1}$ , one obtains

$$\begin{aligned} (H_k^H R_{kk}^{-1} H_k)^{-1} H_k^H R_{kk}^{-1} z_k &= (H_k^H R_{kk}^{-1} H_k)^{-1} H_k^H R_{kk}^{-1} H_k \hat{x} \\ &+ (H_k^H R_{kk}^{-1} H_k)^{-1} H_k^H R_{kk}^{-1} \hat{v}_k \end{aligned}$$

or

$$\hat{\vec{x}}_k = \vec{x} + (H_k^H R_{kk}^{-1} H_k)^{-1} H_k^H R_{kk}^{-1} \vec{v}_k$$

$$\tilde{\vec{x}}_k \triangleq \hat{\vec{x}}_k - \vec{x} = (H_k^H R_{kk}^{-1} H_k)^{-1} H_k^H R_{kk}^{-1} \vec{v}_k$$

or

$$\tilde{\vec{x}}_k = \vec{A}_k^H \vec{v}_k$$

Averaging and assuming independence of  $\vec{A}_k$  and  $\vec{v}_k$ ,  $\tilde{\vec{x}}_k = \vec{A}_k \vec{v}_k = 0$

Hence the estimate  $\tilde{\vec{x}}_k$  is unbiased.

### 3.3 Maximum Likelihood Estimate

The previous derivation minimizes the mean-square error subject to the constraint that a unit plane wave be passed undistorted through the filter. But there is no probabilistic basis for the characteristics of the noise field. In other words, the least squares estimate does not assign probability density functions to the signal or measurement vectors. The derivations are obtained via deterministic arguments only.

It is possible to establish probabilistic arguments if the random process involved is treated as multi-dimensional Gaussian. The corresponding likelihood function can be maximized and thus one arrives at the maximum likelihood principle. The estimated signal vector maximizes the probability of the measurement vector that actually occurs, taking into account the properties of the additive random noise vector.

Consider

$$\vec{z} = H\vec{x} + \vec{v}$$

where  $\vec{z}$  is the measurement vector,  $\vec{x}$  is the true signal vector and  $\vec{v}$  is the random error vector and  $H$  is an appropriate dimensional matrix representing the transformation.

The likelihood function

$$L(\vec{z}, \vec{x}) = P(\vec{z} | \vec{x}) = \frac{P(\vec{z}, \vec{x})}{P(\vec{x})} = \frac{P(\vec{x}, \vec{v})}{P(\vec{x})} \frac{\partial \vec{z}}{\partial \vec{x}}$$

But  $\frac{\partial \vec{z}}{\partial \vec{x}} = 1$ . Therefore,

$$\frac{P(\vec{x}, \vec{v})}{P(\vec{x})} \frac{\partial \vec{z}}{\partial \vec{x}} = \frac{P(\vec{x}, \vec{v})}{P(\vec{x})} = \frac{P(\vec{x}) P(\vec{v})}{P(\vec{x})} = P(\vec{v}) \triangleq P_v(\vec{z} - H\vec{x})$$

$$\frac{\partial L}{\partial \vec{x}} = \frac{P_v(\vec{z} - H\vec{x})}{\partial \vec{x}} = 0$$

The above shows that the likelihood function  $L(\vec{z}, \vec{x})$  which is defined as the probability density function of  $\vec{z}$  conditioned on  $\vec{x}$  is just the density function of  $\vec{v}$  centered around  $H\vec{x}$ .

If  $\vec{v}$  is taken as a zero-mean-Gaussian distributed vector with covariance matrix  $R$ , then

$$P(\vec{z} | \vec{x}) = \frac{1}{(2\pi)^{K/2} |R|^{1/2}} \exp \left[ -\frac{1}{2} (\vec{z} - H\vec{x})^H R^{-1} (\vec{z} - H\vec{x}) \right]$$

Maximizing  $P(\vec{z} | \vec{x})$  is accomplished by minimizing the exponent in brackets with respect to  $\vec{x}$ ; that is  $J = (\vec{z} - H\vec{x})^H R^{-1} (\vec{z} - H\vec{x})$  where the superscript  $H$  denotes complex conjugate transpose.

$$\therefore \frac{\partial J}{\partial \vec{x}^H} = 0$$

or

$$-H^H R^{-1} \vec{z} + H^H R^{-1} H \vec{x} = 0$$

$$\therefore \vec{x} = (H^H R^{-1})^{-1} H^H R^{-1} \vec{z} \quad (3.3.1)$$

and is identical to the weighted least squares estimate. The equivalence of the maximum likelihood estimate for a multi-dimensional Gaussian distribution of the random noise vector and the weighted least square estimate under the constraint that a unit plane wave be passed undistorted through the filter has thus been established.

### 3.4 Estimation of MLM FWPD Spectra

The previous discussion showed; how in general, from a noisy measurement vector, an estimate of the desired signal vector can be obtained such that the sum of the squares of the deviations is a minimum under the "distortion free" constraint. The details of application of the least squares or maximum likelihood principle to the estimation of the FWPD spectrum are set forth in the following.

A unit amplitude signal model is represented by

$$E = \begin{bmatrix} e \\ i2\pi\vec{k} \cdot \vec{r}_1 \\ e \\ i2\pi\vec{k} \cdot \vec{r}_2 \\ \vdots \\ e \\ i2\pi\vec{k} \cdot \vec{r}_n \\ e \end{bmatrix}$$

where  $n$  is the number of sensors in the array  $\vec{r}_n$  is the vector distance to the  $n$ th sensor from an arbitrary origin, and  $\vec{k}$  is the wavenumber vector corresponding to the direction of arrival of the signal. Monochromatic operation is assumed.

If

$$F = \begin{bmatrix} F_1 \\ F_2 \\ \vdots \\ \vdots \\ \vdots \\ F_n \end{bmatrix}$$

is a filter set, then the mean-square error for this filter set is

$$\begin{aligned}\epsilon &= (1-F^H E) (1-E^H F) + F^H S F \\ \epsilon &= 1-E^H F - F^H E + F^H E E^H F + F^H S F\end{aligned}\quad (3.4.1)$$

where  $S$  is the noise cross spectral matrix and the superscript  $H$  denotes the conjugate transpose.

The mean-square-error (MSE) should be minimized subject to the constraint that

$$F^H E E^H F = 1$$

since this represents the filter power output for a unit amplitude plane wave signal model.

This constraint can be incorporated if the expression

$$\epsilon = (1-E^H F) (1-F^H E) + F^H S F + \lambda (F^H E E^H F - 1) \quad (3.4.2)$$

is minimized, where  $\lambda$  is the Lagrangian multiplier.  $\lambda$  can be determined by taking partial derivatives with respect to the real and imaginary components of  $F$ .

Consider the  $m^{\text{th}}$  component of  $F$

$$\begin{aligned}\frac{\partial \epsilon}{\partial \text{Re} F_m} &= -E_m^* (1-F^H E) - E_M (1-E^H F) + (SF)_m \\ &+ (F^H S)_m + \lambda \left[ E_m^* (F^H E) + E_m (E^H F) \right]\end{aligned}$$

and

$$\begin{aligned}\frac{\partial \epsilon}{\partial \text{Im} F_m} &= -i E_m^* (1-F^H E) + i E_m (1-E^H F) \\ &- i (SF)_m + i (F^H S)_m + \lambda \left[ i E_m^* (F^H E) - i E_m (E^H F) \right]\end{aligned}$$

But for an extremum

$$\frac{\partial F}{\partial \operatorname{Re} F_m} + i \frac{\partial \varepsilon}{\partial \operatorname{Im} F_m} = 0 \quad (3.4.3)$$

$$\therefore \varepsilon = -2E_m^H (1 - E_F^H) + 2(SF)_m + 2\lambda E_m^H (E_F^H)$$

$$\therefore SF = E(1 - E_F^H - \lambda E_F^H) \quad (3.4.4)$$

or

$$F = [1 - (\lambda + 1) E_F^H] S^{-1} E$$

$$F^H E E^H F = \left[ F^H E - (\lambda + 1) (F^H E E^H F) \right] E^H S^{-1} E$$

Since  $F^H E E^H F = 1$  (by the constraint).

$$\frac{1}{E^H S^{-1} E} = F^H E - (\lambda + 1)$$

or

$$\lambda + 1 = F^H E + \frac{1}{E^H S^{-1} E}$$

$$SF = E \left[ 1 - (F^H E + \frac{1}{E^H S^{-1} E}) E^H F \right]$$

$$= \frac{E E^H F}{E^H S^{-1} E} \quad (3.4.5)$$

and

$$F^H S F = \frac{F^H E E^H F}{E^H S^{-1} E} = \frac{1}{E^H S^{-1} E}$$

Therefore, the expression for the MSE becomes

$$\epsilon = |1 - E^H F|^2 + \frac{1}{E^H S^{-1} E}$$

and is minimized obviously when  $E^H F = 1 = F^H E$  a condition consistent with  $F^H E E^H F = 1$ .

Since

$$SF = \frac{E E^H F}{E^H S^{-1} E}$$

from Eq. (3.4.5) the filter set which minimizes the MSE is

$$F = S^{-1} E / E^H S^{-1} E \quad (3.4.6)$$

and the minimized noise power

$$F^H S F = \frac{1}{E^H S^{-1} E} \quad (3.4.7)$$

Also  $e^{i\theta} F$  where  $\theta$  is an arbitrary phase factor accomplishes the same task.

The filter  $F$  also maximizes the signal to noise ratio  $G = \frac{F^H E E^H F}{F^H S F}$

without being subjected to the constraint that  $F^H E E^H F = 1$ . Similarly  $C e^{i\theta} F$  would maximize the signal to noise ratio where  $C e^{i\theta}$  is an arbitrary complex valued scalar.

### 3.5 A Relevant Theorem and Additional Properties

The foregoing can be neatly summarized as a theorem involving Hermitian forms,

$$G = \frac{F^H U F}{F^H S F} \quad (3.5.1)$$

If a quantity  $G$  is expressed as a ratio of two Hermitian forms where  $S$  is nonsingular and positive-definite, the largest eigenvalue  $\lambda_M$  of the regular pencil of matrices  $[U-\lambda S]$  is the maximum obtainable  $G$  when  $F$  is the eigenvector satisfying the homoegenous equation

$$UF = \lambda_M SF$$

If  $U$  is expressible as  $U = EE^H$  then the largest and non-zero eigenvalue of the regular pencil  $[U-\lambda S]$  is

$$\lambda_M = G_{MAX} = E^H S^{-1} E \quad (3.5.2)$$

and the eigenvector corresponding to  $\lambda_M$  is

$$F_{MAX} = S^{-1} E \quad (3.5.3)$$

The above equations solve the problem of optimization for spatial processing of array data.

The Hermitian form  $E^H S E$  can be reduced by a unitary transformation  $E = Tx$  to the canonical form

$$\sum_{i=1}^N \lambda_i x_i x_i^H = \sum_{i=1}^N \lambda_i |x_i|^2 \quad (3.5.4)$$

where the  $\lambda$ 's are the eigenvalues of  $S$  and the  $x_i$ 's are the components of  $E$  along the eigenvectors of  $S$ .

Therefore the eigenvalues of  $S^{-1}$  would be

$$(\frac{1}{\lambda_1}, \frac{1}{\lambda_2}, \dots, \frac{1}{\lambda_N})$$

and

$$P_L = \frac{1}{E^H S^{-1} E} = \frac{1}{\frac{|x_1|^2}{\lambda_1} + \frac{|x_2|^2}{\lambda_2} + \dots + \frac{|x_N|^2}{\lambda_N}} \quad (3.5.5)$$

where  $P_L$  is the maximum-likelihood filter output power.

If the probe vector  $E$  lies along the  $j^{\text{th}}$  eigenvector then  $P_L = \lambda_j$  and reflects the correct value of the spectrum.

If  $P_C$  is the conventional filter power output, the relative resolution can be found from the ratio

$$\begin{aligned}
 \frac{P_C}{P_L} &= \left( \sum_i \lambda_i |x_i|^2 \right) \left( \sum_j \frac{|x_j|^2}{\lambda_j} \right) \\
 &= \sum_i \sum_j \frac{\lambda_i}{\lambda_j} |x_i|^2 |x_j|^2 \\
 &= \left( \sum_i |x_i|^2 \right)^2 + \sum_{i \neq j} \frac{\lambda_i}{\lambda_j} |x_i|^2 |x_j|^2 \quad (3.5.6) \\
 &\quad (\text{j is positive real})
 \end{aligned}$$

Therefore,

$$\frac{P_C}{P_L} \geq 1$$

since

$$\left( \sum_i |x_i|^2 \right)^2 = 1$$

Thus, the MLM spectrum has lower output power off the principal axes of the spectral matrix  $S$  and yet  $P_C = P_L$  along the principal axes. The MLM spectrum exhibits sharper peaks and higher resolution. Although this result is not strictly applicable when the eigenvectors of  $S$  lie outside the space spanned by the subset of probe vectors corresponding to wavenumber vectors  $\vec{k}$ , in practice the result is quite robust.

### 3.6 Random Noise and Two Plane Waves

The behavior of the maximum likelihood FWPD spectrum can be analyzed when the noise field consists of a small number of unit plane waves and uncorrelated noise propagating across an array of sensors.

The analysis is based on the assumption that the cross spectral matrix of such a noise field can be represented as

$$S = PI + \sum_{n=1}^N V_n V_n^H \quad (3.6.1)$$

where  $I$  is the unit matrix and  $P$  the variance of the noise.  $V_n V_n^H$  is the  $n^{\text{th}}$  unit plane wave dyadic representation. This representation is a matrix of unit rank. It does not have much physical significance when a large number of plane waves are present.

Consider the case of two complex sinusoids and white noise. Then

$$S = PI + UU^H + VV^H$$

where

$$U = a \times \text{col}(e^{i2\pi \vec{k}_u \cdot x_1}, e^{i2\pi \vec{k}_u \cdot x_2}, \dots)$$

and

$$V = b \times \text{col}(e^{i2\pi \vec{k}_v \cdot x_1}, e^{i2\pi \vec{k}_v \cdot x_2}, \dots)$$

$\vec{k}_u$  and  $\vec{k}_v$  representing the wavenumbers for the two plane waves.

Therefore, the MLM spectrum can be shown to be

$$\frac{1}{E^H S^{-1} E} = \frac{P \begin{vmatrix} P + |U|^2 & U^H V \\ V^H & P + |V|^2 \end{vmatrix}}{\begin{vmatrix} |E|^2 & E^H U & E^H V \\ V^H E & P + |U|^2 & U^H V \\ V^H E & V^H U & P + |V|^2 \end{vmatrix}}$$

from which  $\lim_{p \rightarrow 0} \frac{1}{E^H S^{-1} E} = 0$  if  $E \neq \alpha U + \beta V$  where  $\alpha$  and  $\beta$  are complex-valued scalars.

In particular if  $E = U/|U|$

$$\lim_{p \rightarrow 0} \frac{1}{E^H S^{-1} E} = |U|^2$$

and if  $E = V/|V|$

$$\lim_{p \rightarrow 0} \frac{1}{E^H S^{-1} E} = |V|^2$$

Therefore, the spectrum exhibits a type of pseudolinearity in the vicinity of the directions of  $U$  and  $V$  provided  $P$  is small. The conventional estimate  $E^H S E$  yields

$$\lim_{p \rightarrow 0} E^H S E = |U|^2 + \frac{|U^H V|^2}{|U|^2}$$

if

$$E = \frac{U}{|U|}$$

and

$$V^2 + \frac{|V^H U|^2}{|V^2|}$$

if

$$E = \frac{V}{|V|}$$

The MLM spectrum gives the true value of  $U$  and  $V$  when the steering vector points in either of these directions whereas the conventional estimate is corrupted by the influence of  $U$  while pointed towards  $V$  and vice versa. At all other points  $E$ , not a linear combination of  $U$  and  $V$ , the spectrum tends to zero when  $P$  is small.

In the case of a single complex sinusoid if

$$E = \frac{V}{|V|}$$

then

$$\lim_{p \rightarrow 0} \frac{1}{E^H S^{-1} E} = |V|^2$$

and

$$\lim_{p \rightarrow 0} E^H S E = |V|^2$$

whereas if  $E \neq \alpha V$

$$\lim_{p \rightarrow 0} \frac{1}{E^H S^{-1} E} = 0$$

but

$$\lim_{p \rightarrow 0} E^H S E = |U^H V|^2$$

reflecting the window effect.

### 3.7 Computational Procedure

The computational procedure is set forth in the following steps.

The normalized input Fourier spectra from the various antennas is converted to cross-spectral estimates  $\hat{S}_{jm}(w)$  by anyone of several spectral estimation procedures, in this case by frequency averaging and smoothing with seven frequencies. Subscripts  $j$  and  $m$  refer to the antennas in question. Next an  $N \times N$  matrix of cross-spectral estimates  $[\hat{S}(w)]$  is organized at each  $w$ , where  $N$  is the total number of antennas. Not all  $N \times N$  terms need be evaluated since  $S_{jm}(w) = S_{mj}^*(w)$ , where the asterisk denotes complex conjugation. The sum of the diagonal elements

in the matrix is stored as a measure of total power at any given Doppler frequency and used for renormalization purposes ultimately. The matrix itself is normalized by replacing each element  $S_{jm}(w)$  by  $\hat{S}_{jm}(w) / \sqrt{\hat{S}_{jj}(w)\hat{S}_{mm}(w)}$ , a step which ensures sensor equalization. The normalized cross-spectral matrix is inverted for each Doppler frequency one at a time. The elements of the inverted matrix are used in the equation for f-k spectra

$$\hat{P}(w, \vec{k}) = \left[ \sum_{m=1}^N \sum_{n=1}^N [S_{jm}]^{-1} \exp ik \cdot (r_j - r_m) \right]^{-1}$$

It is seen that the weights  $w_i$  and the straightforward cross-spectral elements together are replaced by the corresponding inverted matrix elements and the reciprocal is calculated to yield the high-resolution f-k estimate. The increments over  $k$  are calculated in a chain sequence from the previous values in the same manner as indicated before. The final step is to restore relative power levels at the different Doppler frequencies. First, the values of  $\hat{P}(w, k)$  are summed over all  $k$  and the normalized values of  $\hat{P}(w, k)$  are multiplied by the sum of the diagonal elements  $P_{ds}(w)$  of the original cross-spectral matrix which have been stored as indicated before. Thus, the renormalized  $\hat{P}(w, k)$  are obtained and with an appropriate scale factor and conversion to a digicoder format are recorded on tape to produce the digicoder printouts.

## 4. RESULTS

### 4.1 Simulated Models of Signals and Random Noise

This section discusses the results of the application of the maximum likelihood method to simulated models of signals and white noise generated in complex valued digital form on the computer. The signal part of the test function is modeled as the sum of one or more complex sinusoids with appropriate progressive phase shifts along the linear array. Thus, if two sources on two different Doppler angular frequencies  $w_1$  and  $w_2$  and located in directions  $\theta_1$  and  $\theta_2$  from the axis of the array have to be simulated, the expression

$$s_n(t) = A_1 \exp j(w_1 t + \frac{2\pi}{\lambda} d_n \cos \theta_1)$$

$$+ A_2 \exp j(w_2 t + \frac{2\pi}{\lambda} d_n \cos \theta_2)$$

is used. Here  $A_1$  and  $A_2$  are the respective amplitudes of the two sinusoids,  $\lambda$  is the operating wavelength of the r.f carrier, and the subscript  $n$  is the antenna index,  $d_n$  being the distance of the  $n^{\text{th}}$  antenna from the origin. The value of  $s_n(t)$  is calculated at discrete equally spaced time points  $t_1, t_2, \text{ etc.}$ , to obtain the sampled data points.

Additive white noise is introduced by appropriately scaled random numbers from a random function generator. The scaling determines the amount of noise power added. The sampled data points along with the noise is processed as described earlier to produce DAASM maps.

### 4.2 Parameter Variations and Digicoder Displays

The performance of the MLM was studied with test functions designed to vary the following parameters.

- 1) Several noise levels (Figs. 1-10)
- 2) Different number of Doppler frequencies being smoothed (Fig. 1)
- 3) Number of sources:
  - a) coherent (same Doppler) (Figs. 8 & 10)
  - b) incoherent (separated Dopplers) (Figs. 2, 3, 4, 5, 6, 7 & 9)

- 4) Proximity of sources
  - a) wavenumber (Figs. 4, 5)
  - b) Doppler frequency (Figs. 2, 3, 9)
- 5) Number of antennas either 6 or 12 & configuration
  - a) uniform (Figs. 1, 2, 3, 4, 5, 6, 7)
  - b) minimum redundancy (Figs. 6, 7, 9, 10)

Salient results pertaining to the above variations are presented here in the form of digicoder plots of Doppler frequency against wavenumber (angle of arrival). Tables 1 - 10, provides the details of the parameters in each plot.

The digicoder plot is designed so that there are 128 Doppler frequency lines and 128 wavenumber lines. Since the width of the digicoder printout can accommodate 256 lines two different cases can be presented on the same plot, one in the left half and the other in the right half.

The characters represent numbers from 0 to 15 in increasing order of intensity and as described before logarithmically scaled from the corresponding linear values of the spectra. In effect, the digicoder plot is also an intensity plot. Sixteen preface lines precede the actual plot and are utilized to code all relevant information about the parameters. Also, this space is divided into 16 compartments across the full font for viewing ease. A similar compartmentalization is effected along the length of the page by interrupting the plot with a preface line every 16 lines.

In the plots presented here the wavenumber axis is across the width of the page and Doppler frequency along the length. The wavenumber axis corresponds to an azimuthal direction of arrival between  $-90^\circ$  and  $+90^\circ$  with  $0^\circ$  corresponding to boresight. Actually any sector of the azimuthal coverage can be expanded to occupy the full 128 lines. Similarly, the middle of the Doppler axis represents 0 Hz becoming increasingly negative towards the top and increasingly positive towards the bottom. Once again, any portion of the Doppler spectrum with any chosen center frequency can be accommodated.

It should be noted that the wavenumber axis represents the sine of the angle away from boresight. Therefore, the angles corresponding to the horizon are compressed although approximately linear in the region of boresight.

## 5. CONCLUSIONS

### 5.1 Incoherent Sources

Computations have been made with the noise levels corresponding to power S/N ratios of 20 dB, 10 dB, 0 dB, and -5 dB. In the case of incoherent sources assuming the large aperture, the estimate is very accurate at low noise levels and the accuracy is maintained even at angles close to the horizon as seen in Figs. 6, 7 & 9d, e & f. As long as the sources do not overlap in Doppler for a specified smoothing they can be resolved to within  $1^\circ$ . As the noise level is increased, this resolution cannot be maintained and slight shifts in angular position are observed. The valleys between the peaks do not quite bottom out to the low value reached at angles away from the source locations. Also, as the noise level is increased apart from the noise appearing randomly at all Dopplers and all angles, the angular side lobes on the signal Doppler frequency form a ridge. The ridge is particularly obvious when the line source happens to be off the lines on the MLM spectra actually computed and is attributable to the procedure for renormalization of power across the Doppler frequencies as seen in Fig. 4. The ridge effect vanishes when the source is distributed over wavenumber, since in that instance, no single line contributes inordinately to the total power in the Doppler line and hence, the actually computed adjacent lines are as effective.

There is a definite relationship between the number of frequencies that are used for smoothing and the number of antennas (sensors) employed. In general, no problems are encountered in the way of singular spectral matrices if the number of frequencies exceeds twice the number of sensors. But for longer arrays this procedure is impractical. An alternate solution to avoiding singular spectral matrices would be to add a small correction term  $\Delta$  to the diagonal terms of the normalized cross-spectral matrix.

The above implies that resolution in Doppler has to be compromised to achieve improved angular resolution. As one increases the number of spatial points at which the incident noise field is measured, one can afford to add a little noise to the diagonal terms. For this reason, a 15 point smoothed frequency averaging is employed thus allowing adequate Doppler resolution (Ref. Figs. 3-10). In fact, it was observed that 5 point frequency smoothing

resulted in ill conditioned matrices for the 6-antenna mode while 7-frequency smoothing was marginal (Ref. Fig. 2). The successful inversion of 7-frequency smoothed cross-spectral matrices can be attributed to the noise added in the original time series. In comparison, the twelve antenna mode cross-spectral matrices could only be inverted for 11 or more points smoothing.

A similar argument can be advanced as to the ideal location of the antennas. For instance, a small number of antennas can be placed in a minimum redundancy configuration provided more time samples are available to maintain a decent signal-to-noise ratio. A more reliable estimate can then be obtained. In a certain restricted sense, the spatial and temporal points are interchangeable. Conversely, redundancy in available distances between pairs of antennas in a uniformly spaced array provides a better estimate in the presence of noise. If angular resolution is the primary objective, it is advisable to utilize the maximum possible aperture consistent with requirements of spatial coherence. For a given amount of frequency averaging, this would entail a sacrifice in the stability of the estimates.

It is observed that there is coupling between the sources even though they are on different Doppler frequencies beyond the bandpass edges of the smoothing filter. The problem seems to be accentuated at low noise levels and small apertures (Ref. Fig. 5). If the spillover pips are above the background noise levels the method exhibits ambiguity as to the location of the sources corresponding to a particular Doppler frequency. When the background noise level obscures the weakly coupled source, this phenomenon vanishes. The explanation for the stronger coupling in the case of smaller apertures can be traced to the wider beamwidth, and hence decreased resolution.

However, this coupling phenomenon does not seem to be of much concern in the case of actual measured data of the DAASM experiment because the noise levels are such as to submerge the level of the coupled signal.

## 5.2 Coherent Sources

Thus far, the results discussed pertain to the case of incoherent sources and the technique suffers from no serious difficulties. When the input data

results from coherent discrete sources, the sidelobes in wavenumber space reach disconcerting levels (Ref. Figs. 8 & 10). In general, it is seen that two sources of equal amplitudes result in an apparent sidelobe level of approximately -6 dB or higher. This imposes quite a degree of uncertainty in being able to distinguish between strong and weak sources. The sidelobes could be mistaken for weak sources or vice versa. Nevertheless, under similar circumstances the conventional FWPD spectrum behaves even worse, true to the theoretical predictions of the last Chapter. The ability to discriminate between the two coherent sources also deteriorates as the noise increases. The situation is improved, but not very much when the number of antennas is increased from 6 to 12 (compare Fig. 8 with Fig. 10).

The angular separation of the sources beyond the natural beamwidth for any given aperture does not seem to provide any readily predictable pattern of sidelobe location or level. The source locations are still discernible with a priori knowledge but in the case of actual data, for instance coherent groundscatter returns, it is extremely difficult if not impossible to locate the authentic reflection points.

It is evident that the case of multiple coherent sources has to be solved by either imposing additional constraints or by decoupling the sources. Imposing additional constraints would require a priori knowledge of the location of the sources which is impractical. In a real environment, the location of interferers may change or the ionospheric conditions may result in multipath propagation leading to apparent multiple-source-type strongly coherent signals.

A method of decoupling the sources utilizing adaptive feedback techniques can be employed. An initial run would yield the approximate location of true as well as virtual sources based on a decision oriented analysis. A decoupling matrix can then be constructed which in turn would be incorporated into the input cross-spectral matrix for each wavenumber of interest. The output would then conform to just one source location as though all the other sources were not present, which should result in very low sidelobe level.

The MLM FWPD spectrum has been previously used in seismological applications. But the application of the technique to the analysis of ionospheric motion and irregularities is thought to be new. It is a powerful technique with superior resolution, is data-adaptive and computationally not much more complex than conventional methods.

T A B L E S  
A N D  
I L L U S T R A T I O N S

TABLE 1.

## Legend for Fig. 1 (Effect of Smoothing)

Figs.	a	b	c	d	e	f
Antenna Array; U = uniform	U	U	U	U	U	U
Number of Antennas	6	6	6	6	6	6
Antenna Aperture (Wavelengths)	<3	<3	<3	<3	<3	<3
Doppler Lines (No.)	59	59	59	59	59	59
Noise Level as % of Signal on Line 59	10	100	300	10	100	300
Doppler Smoothing, No. of Points	7	7	7	15	15	15
Spatial Angle of Source from Boresight.	-30°	-30°	-30°	-30°	-30°	-30°

Reproduced from  
best available copy.

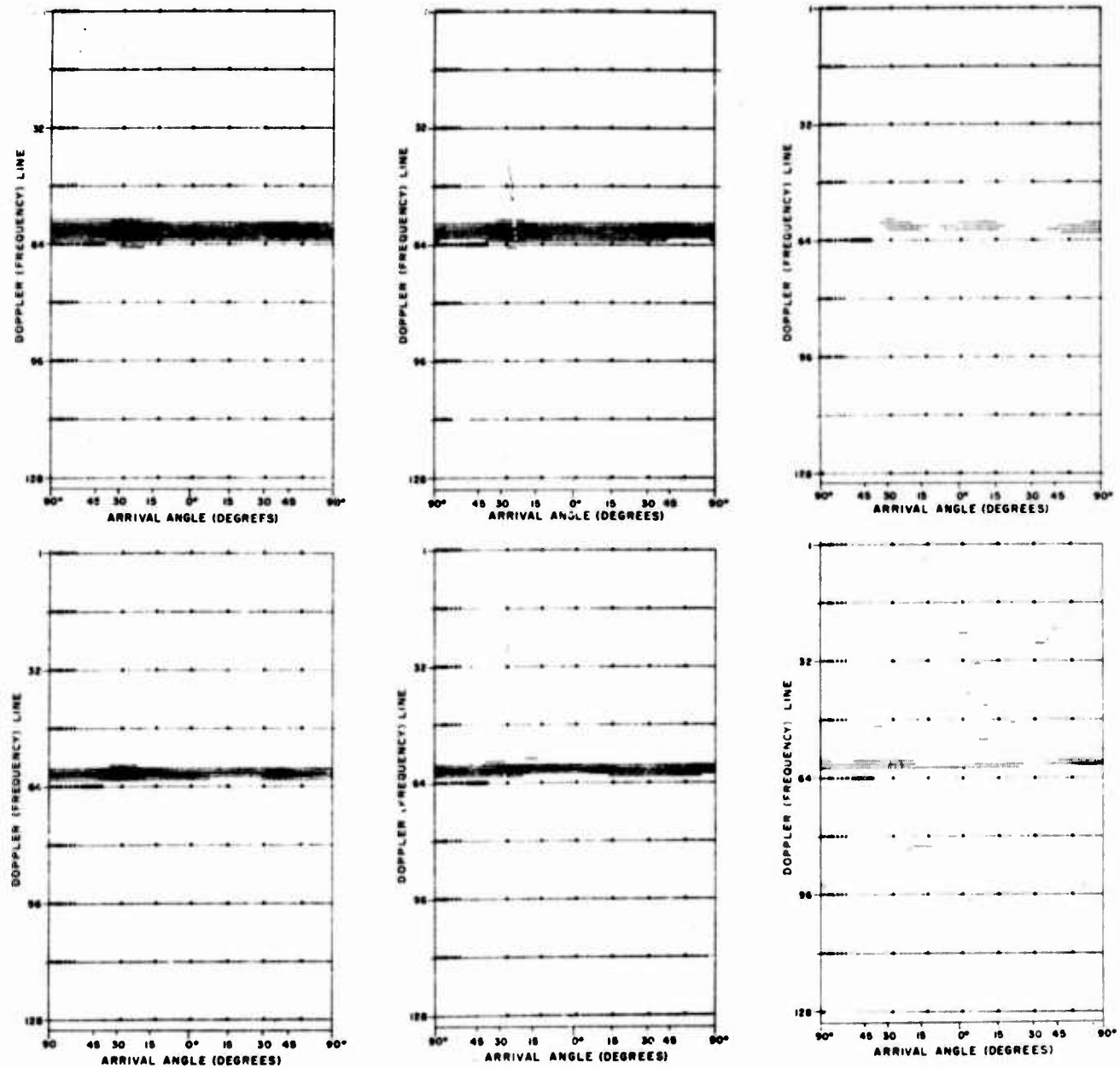


Fig. 1 d e f  
a b c

TABLE 2.

## Legend for Fig. 2 (Doppler Proximity)

Figs.	a	b	c	d	e	f
Antenna Array; U = uniform	U	U	U	U	U	U
Number of Antennas	6	6	6	6	6	6
Antenna Aperture (Wavelengths)	<3	<3	<3	<3	<3	<3
Doppler Lines (No.)	24,59	24,59	24,59	44,59	44,59	44,59
Noise Level as % of Signal on Line 59	10	100	300	10	100	300
Doppler Smoothing, No. of Points	7	7	7	7	7	7
Spatial Angle of Sources from Boresight.	$0^\circ, -30^\circ$					

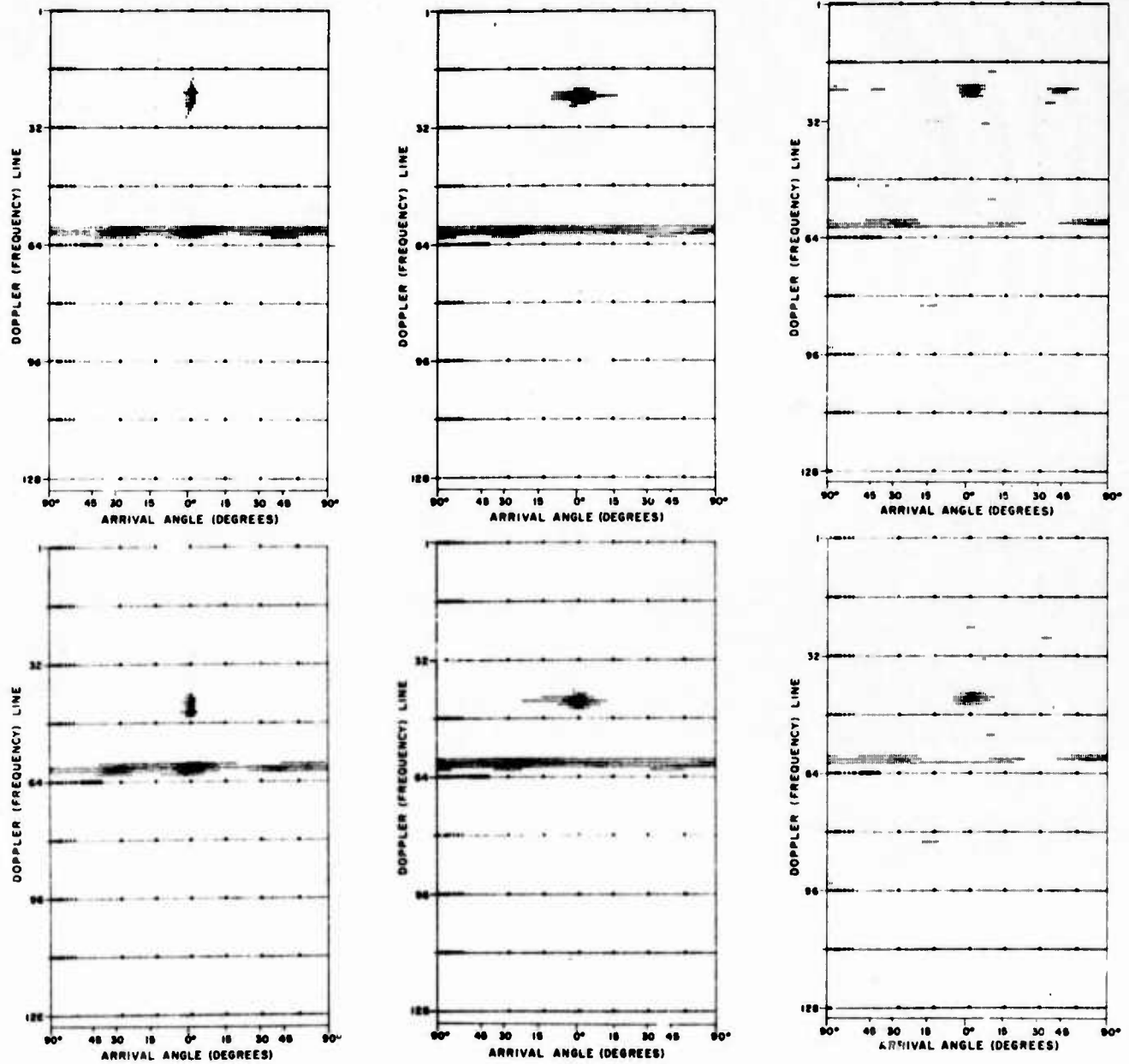


Fig. 2 a b c  
d e f

TABLE 3.

## Legend for Fig. 3 (Doppler Proximity)

Figs.	a	b	c	d	e	f
Antenna Array; U = uniform	U	U	U	U	U	U
Number of Antennas	6	6	6	6	6	6
Antenna Aperture (Wavelengths)	<3	<3	<3	<3	<3	<3
Doppler Lines (No.)	24,59	24,59	24,59	44,59	44,59	44,59
Noise Level as % of Signal on Line 5°	10	100	300	10	100	300
Doppler Smoothing, No. of Points	15	15	15	15	15	15
Spatial Angle of Sources from Boresight.	0°, -30°	0°, -30°	0°, -30°	0°, -30°	0°, -30°	0°, -30°

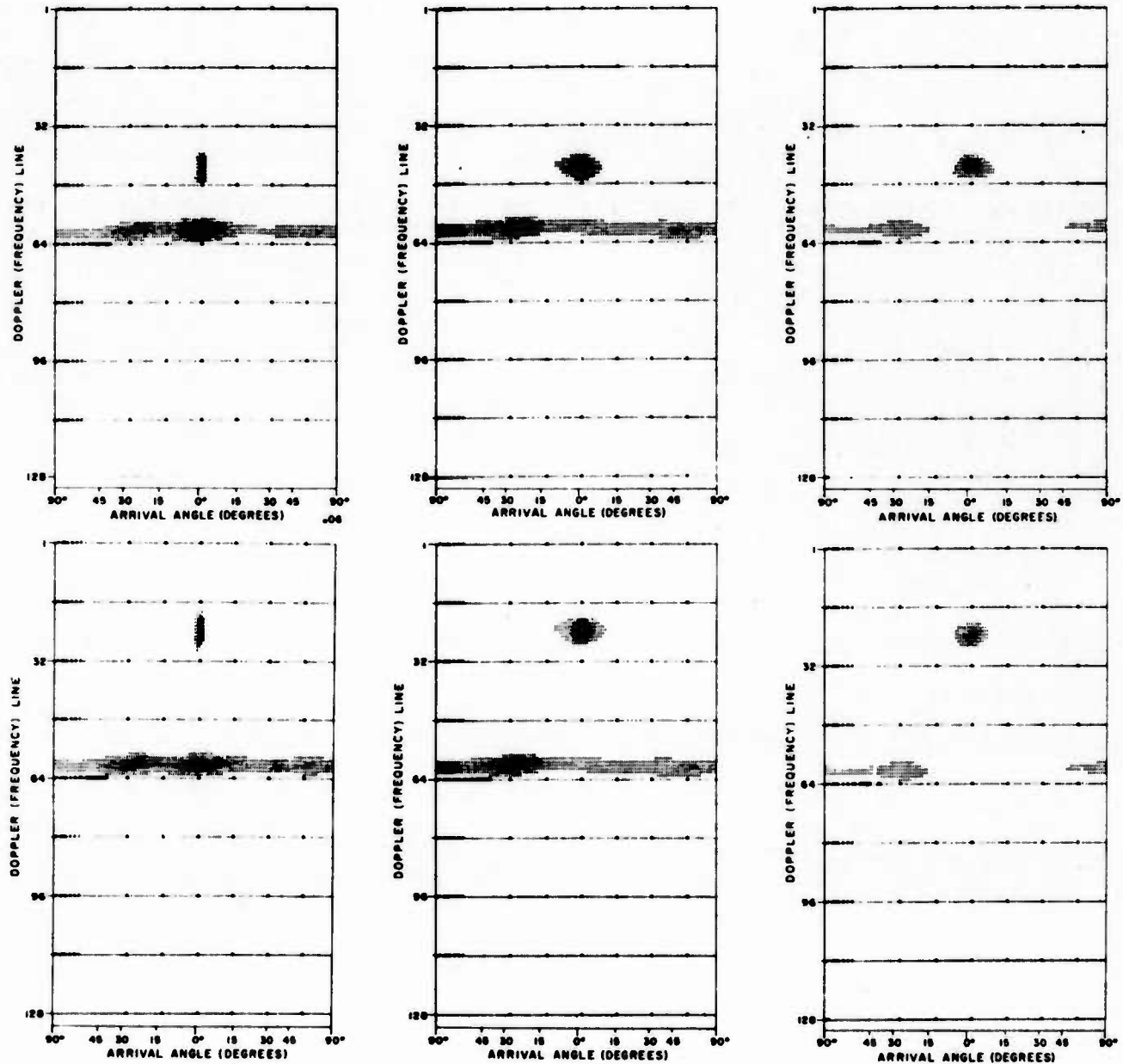


Fig. 3 d e f  
a b c

TABLE 4.

Legend for Fig. 4 (Angular Proximity, Incoherent Sources)

Figs.	a	b	c	d	e	f
Antenna Array; U = uniform	U	U	U	U	U	U
Number of Antennas	6	6	6	6	6	6
Antenna Aperture (Wavelengths)	<3	<3	<3	<3	<3	<3
Doppler Lines (No.)	24,59	24,59	24,59	24,59	24,59	24,59
Noise Level as % of Signal on Line 59	10	100	300	10	100	300
Doppler Smoothing, No. of Points	15	15	15	15	15	15
Spatial Angle of Sources from Boresight.	0°,-30°	0°,-30°	0°,-30°	20°,-30°	20°,-30°	20°,-30°

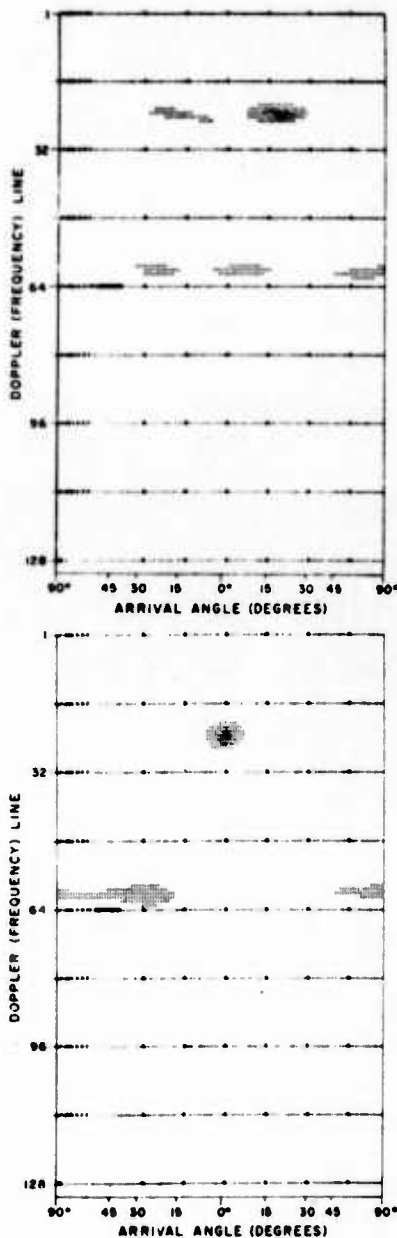
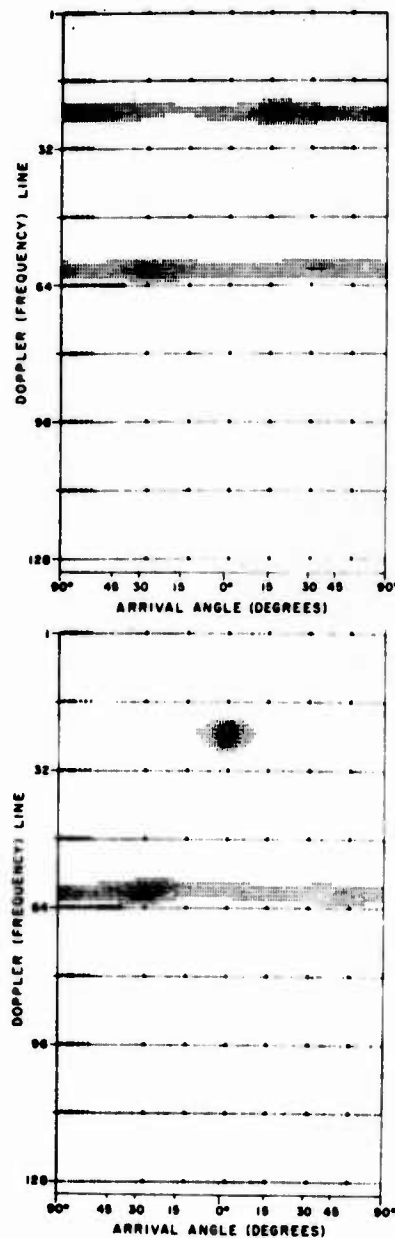
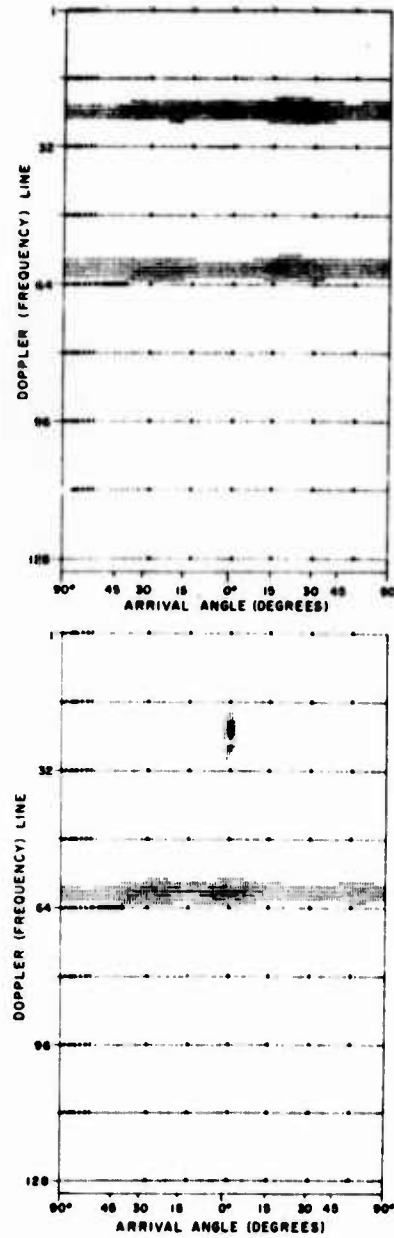


Fig. 4 d e f  
a b c

TABLE 5.

Legend for Fig. 5 (Angular Proximity, Incoherent Sources)

Figs.	a	b	c	d	e	f
Antenna Array; U = uniform	U	U	U	U	U	U
Number of Antennas	6	6	6	6	6	6
Antenna Aperture (Wavelengths)	<3	<3	<3	<3	<3	<3
Doppler Lines (No.)	44,59	44,59	44,59	44,59	44,59	44,59
Noise Level as % of Signal on Line 59	10	100	300	10	100	300
Doppler Smoothing, No. of Points	15	15	15	15	15	15
Spatial Angle of Sources from Boresight.	0°, -30°	0°, -30°	0°, -30°	20°, -30°	20°, -30°	20°, -30°

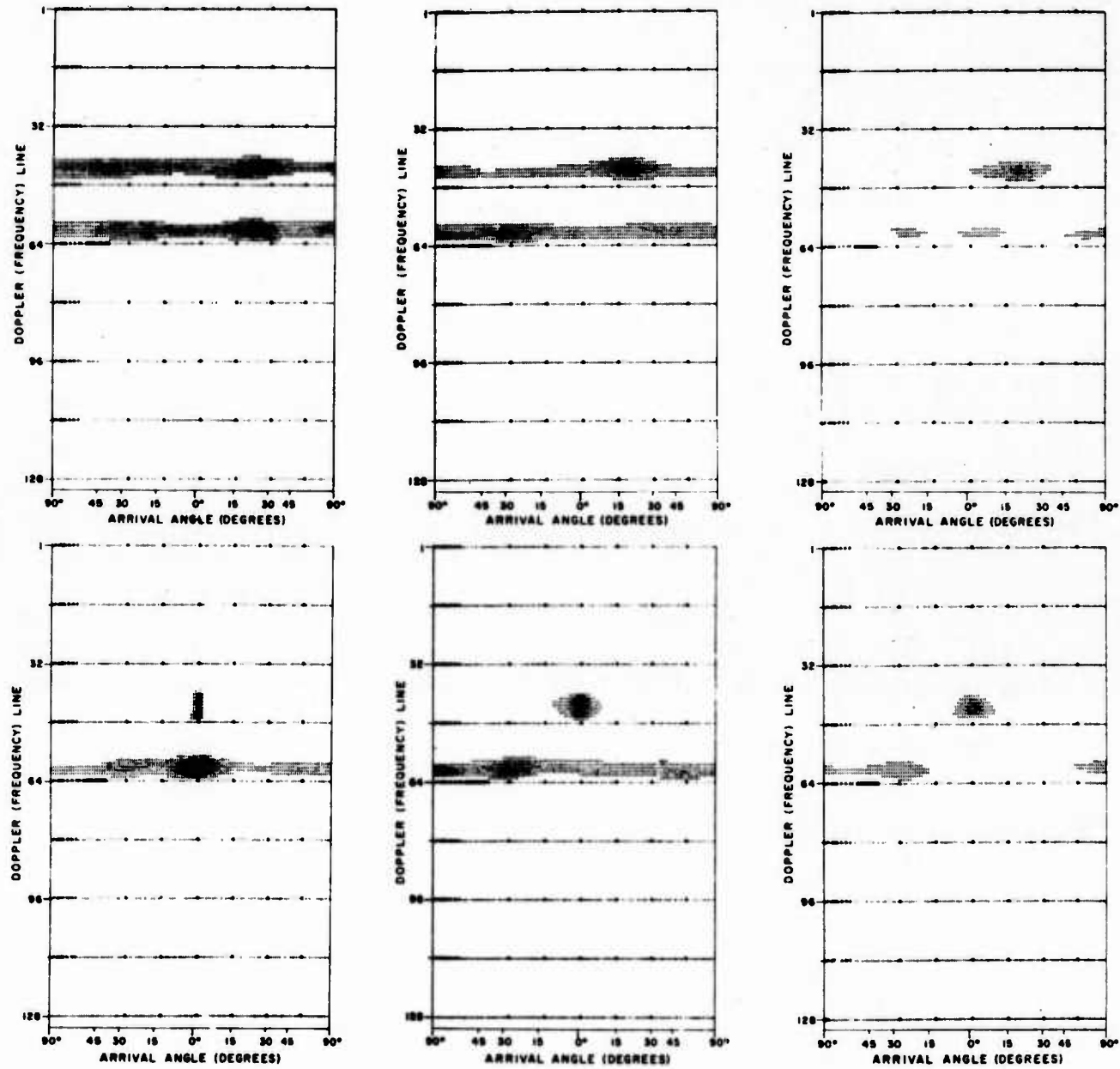


Fig. 5 d e f  
a b c

TABLE 6.

## Legend for Fig. 6 (Antenna Configurations)

Figs.	a	b	c	d	e	f
Antenna Array; U = uniform, MR = minimum redundancy	U	U	U	MR	MR	MR
Number of Antennas	6	6	6	6	6	6
Antenna Aperture (Wavelengths)	<3	<3	<3	>20	>20	>20
Doppler Lines (No.)	24,59	24,59	24,59	24,59	24,59	24,59
Noise Level as % of Signal on Line 59	10	100	300	10	100	300
Doppler Smoothing, No. of Points	15	15	15	15	15	15
Spatial Angle of Sources from Boresight.	0°, -30°	0°, -30°	0°, -30°	0°, -30°	0°, -30°	0°, -30°

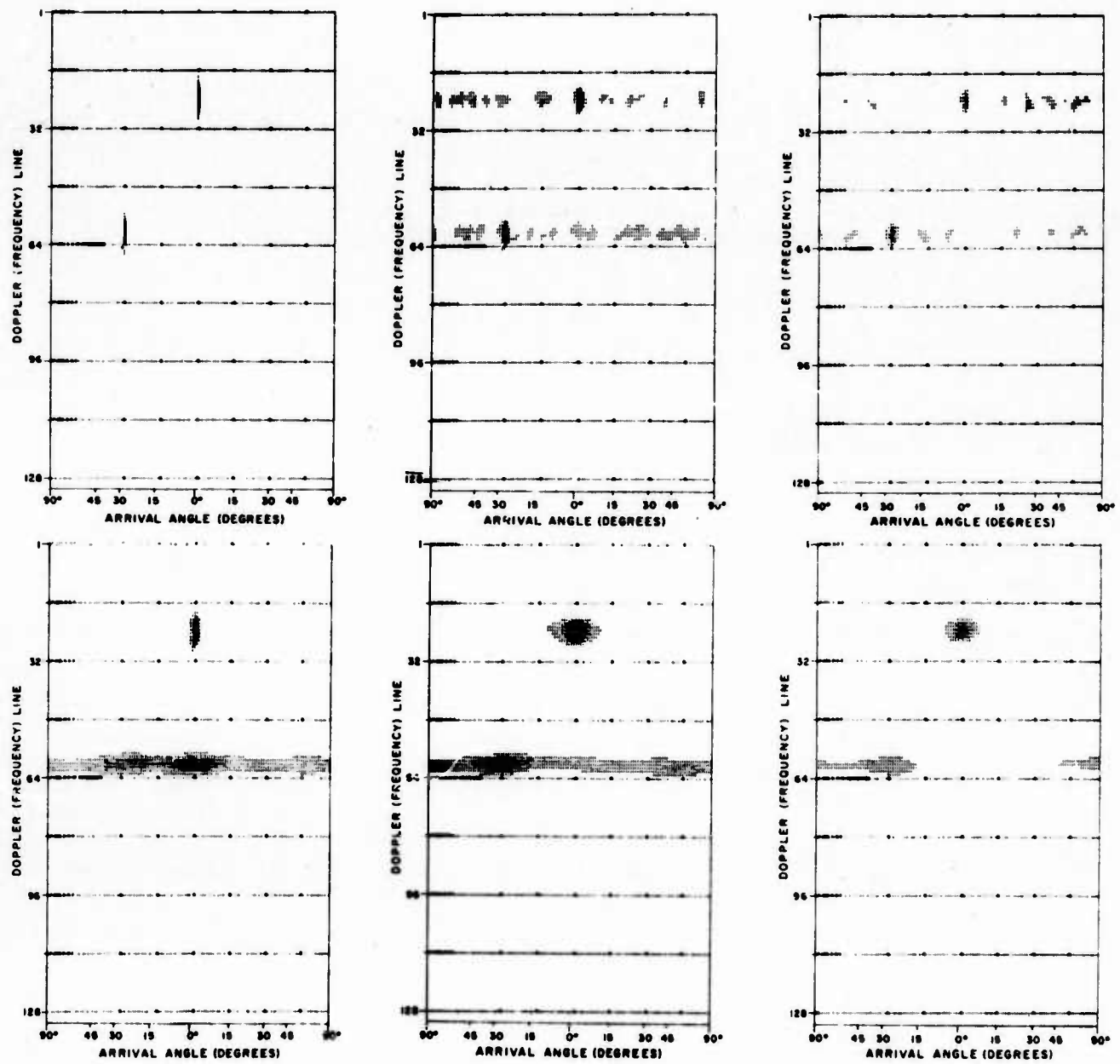


Fig. 6 d e f  
a b c

TABLE 7.

## Legend for Fig. 7 (Antenna Configurations)

Figs.	a	b	c	d	e	f
Antenna Array; U = uniform, MR = minimum redundancy	U	U	U	MR	MR	MR
Number of Antennas	6	6	6	6	6	6
Antenna Aperture (Wavelengths)	<3	<3	<3	>20	>20	>20
Doppler Lines (No.)	44,59	44,59	44,59	44,59	44,59	44,59
Noise Level as % of Signal on Line 59	10	100	300	10	100	300
Doppler Smoothing, No. of Points	15	15	15	15	15	15
Spatial Angle of Sources from Boresight.	0°, -30°	0°, -30°	0°, -30°	0°, -30°	0°, -30°	0°, -30°

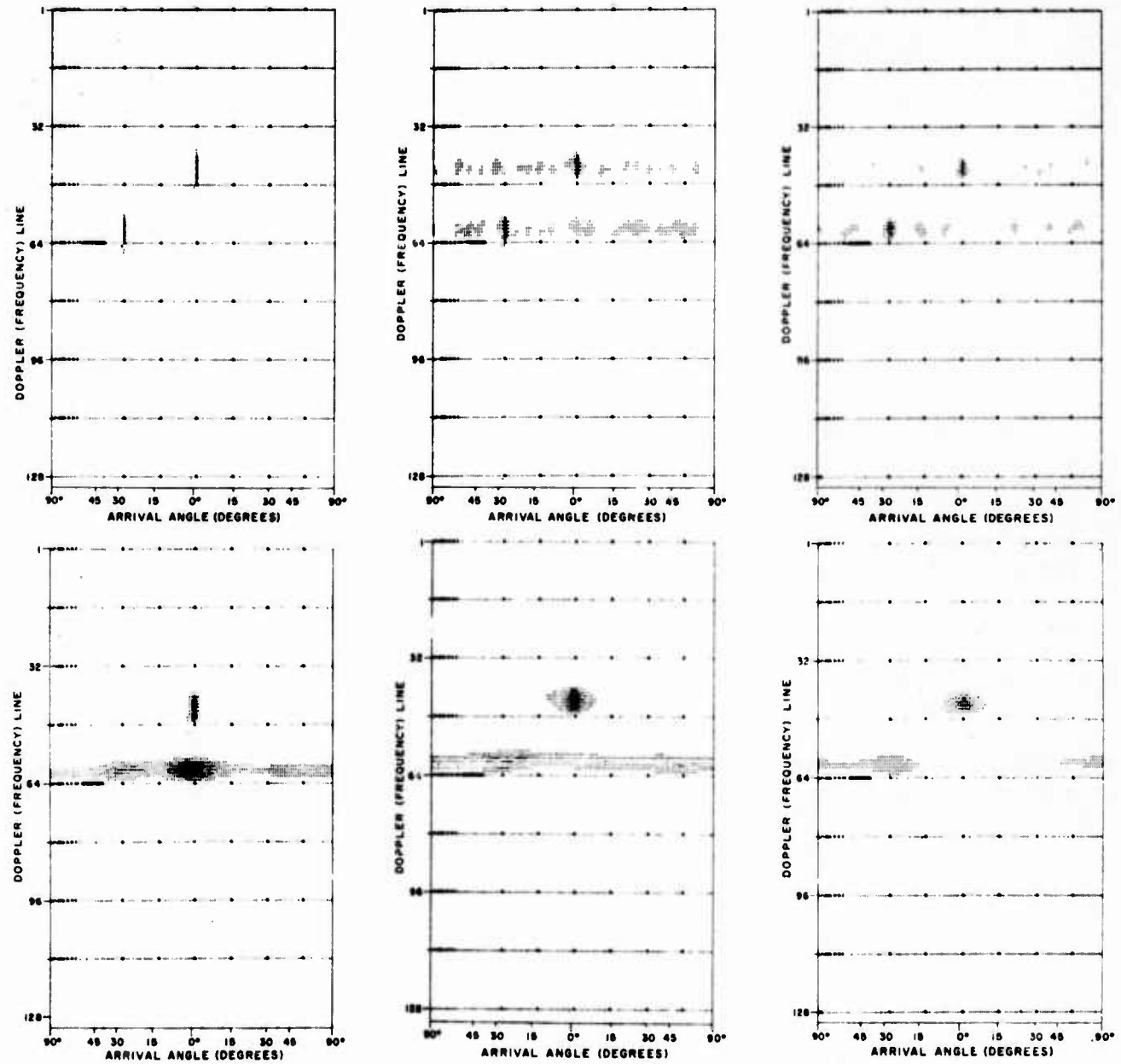


Fig. 7 d e f  
a b c

TABLE 8.

## Legend for Fig. 8 (Coherent Sources)

Figs.	a	b	c	d	e	f
Antenna Array; U = uniform, MR = minimum redundancy	U	U	U	MR	MR	MR
Number of Antennas	6	6	6	6	6	6
Antenna Aperture (Wavelengths)	<3	<3	<3	>20	>20	>20
Doppler Lines (No.)	59	59	59	59	59	59
Noise Level as % of Signal on Line 59	10	100	300	10	100	300
Spatial Angle of Sources from Boresight.	$0^\circ, -30^\circ$					

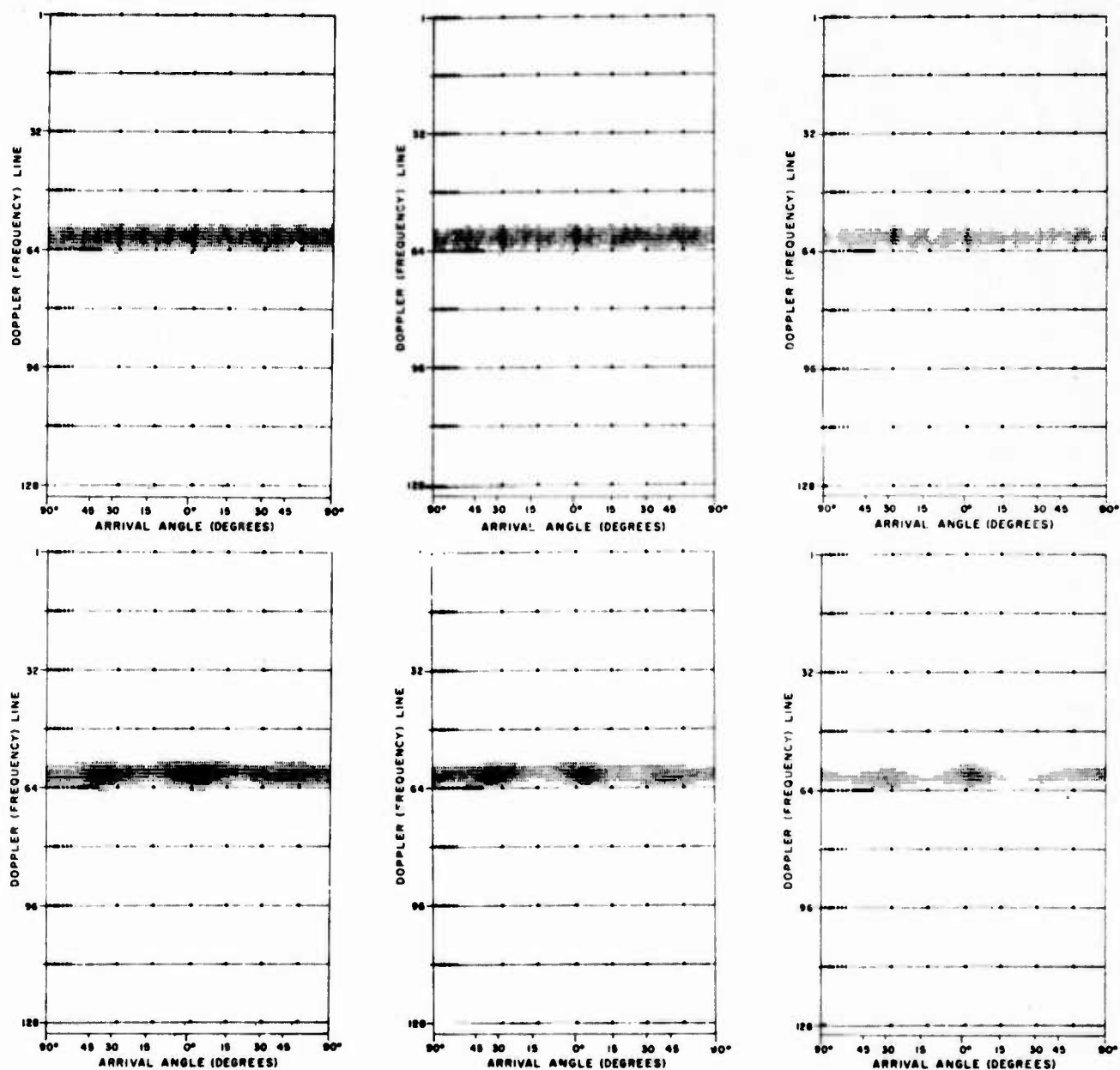


Fig. 8    d e f  
a b c

TABLE 9.

## Legend for Fig. 9 (Antenna Configuration)

Figs.	a	b	c	d	e	f
Antenna Array; U = uniform MR = minimum redundancy	U	U	U	MR	MR	MR
Number of Antennas	12	12	12	11	11	11
Antenna Aperture (Wavelengths)	<3	<3	<3	>20	>20	>20
Doppler Lines (No.)	44,59	44,59	44,59	44,59	44,59	44,59
Noise Level as % of Signal on Line 59	10	100	300	10	100	300
Spatial Angle of Sources from Boresight.	0°, -30°	0°, -30°	0°, -30°	0°, -30°	0°, -30°	0°, -30°

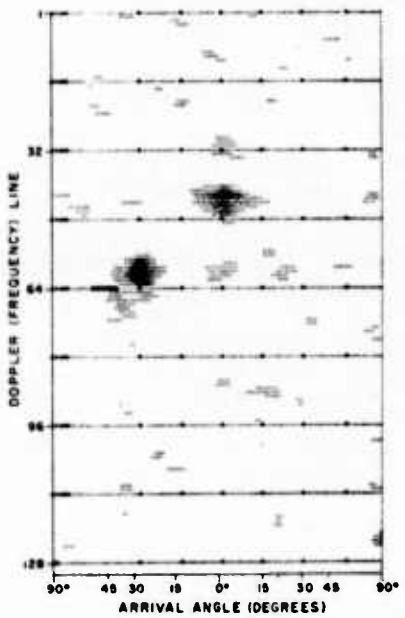
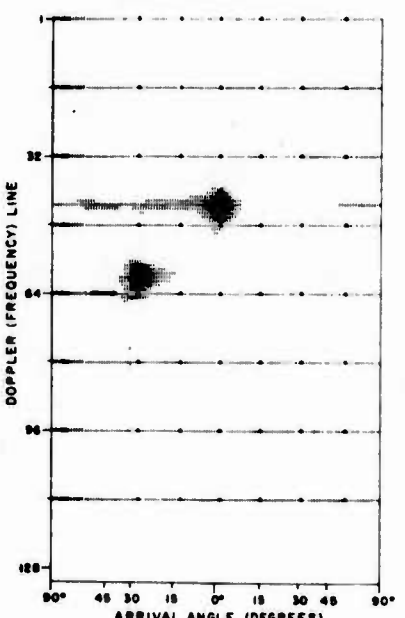
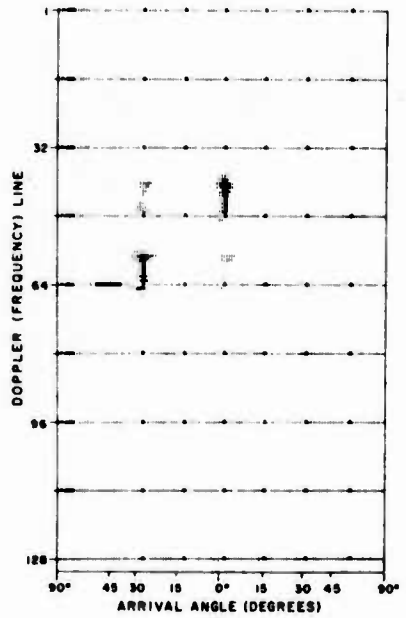
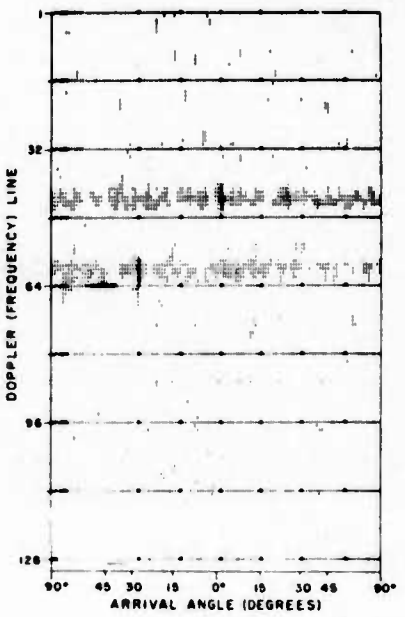
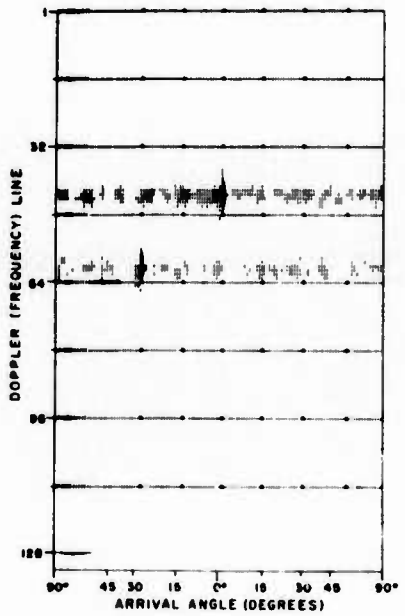
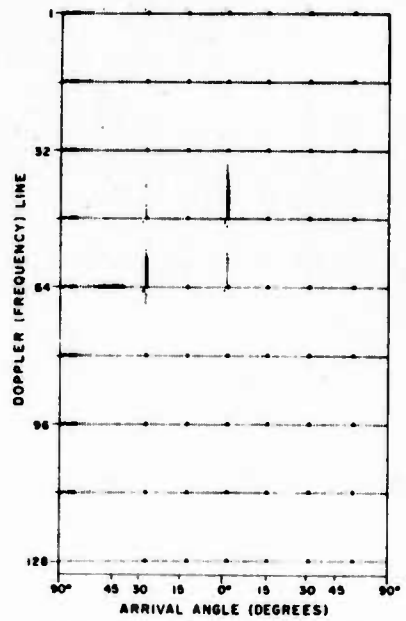


Fig. 9    d e f  
a b c

TABLE 10.

## Legend for Fig. 10 (Coherent Sources)

Figs.	a	b	c	d	e	f
Antenna Array; U = uniform MR = minimum redundancy	U	U	U	MR	MR	MR
Number of Antennas	12	12	12	11	11	11
Antenna Aperture (Wavelengths)	<3	<3	<3	>20	>20	>20
Doppler Lines (No.)	59	59	59	59	59	59
Noise Level as % of Signal on Line 59	10	100	300	10	100	300
Spatial Angle of Sources from Boresight.	0°, -30°	0°, -30°	0°, -30°	0°, -30°	0°, -30°	0°, -30°

Reproduced from  
best available copy. C

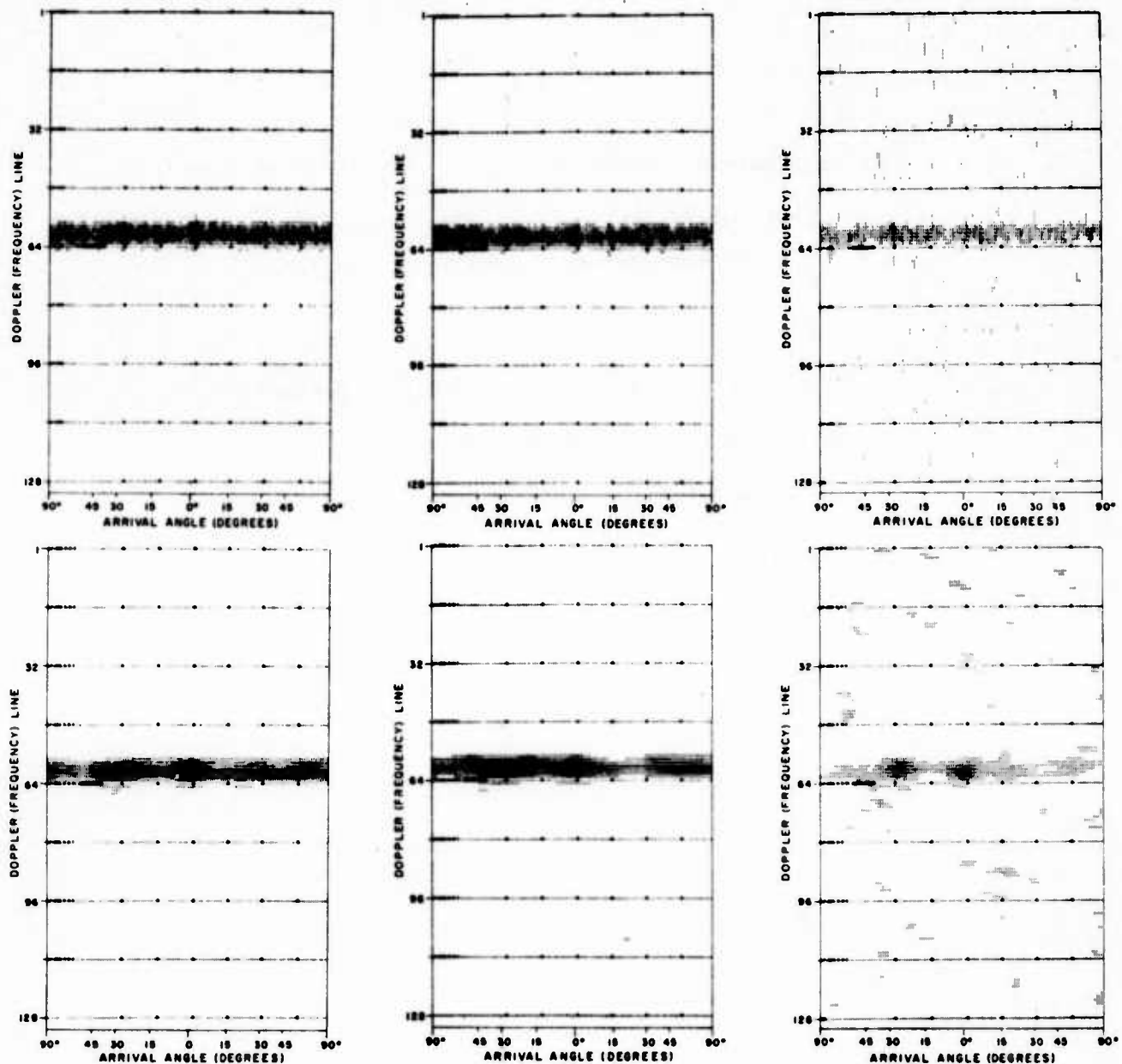


Fig. 10 d e f  
a b c

TABLE 11.

For Data Sample: Flight 4-196, 15 July 1974, UT 2100

See: DAASM Map, p. 98 - ref. report\*

Coherence Map, p. 99 - ref. report\*

Antenna Array - Minimum Redundancy, 6 Antennas

Antenna Aperture -- 720 Meters

Doppler Smoothing, No. of Points -- 15

Freq 1 (MHz) -- 8.22 Figs. a, b, c

Freq 2 (MHz) -- 6.62 Figs. d, e, f

Range (KM) -- 960

Azimuth (deg) -- 349T

Center Freq (Hz) -- +6

Power Spectra: Figures a & d

Coherence Spectra: Figures b & e

DAASM Maps, F-K Spectra: Figures c & f

\* Sales, G.S., et al (1975) DAASM Project - High Latitude Aircraft HF Propagation Experiment, AFCRL-TR-75-0290, Environmental Res. Papers, No. 516

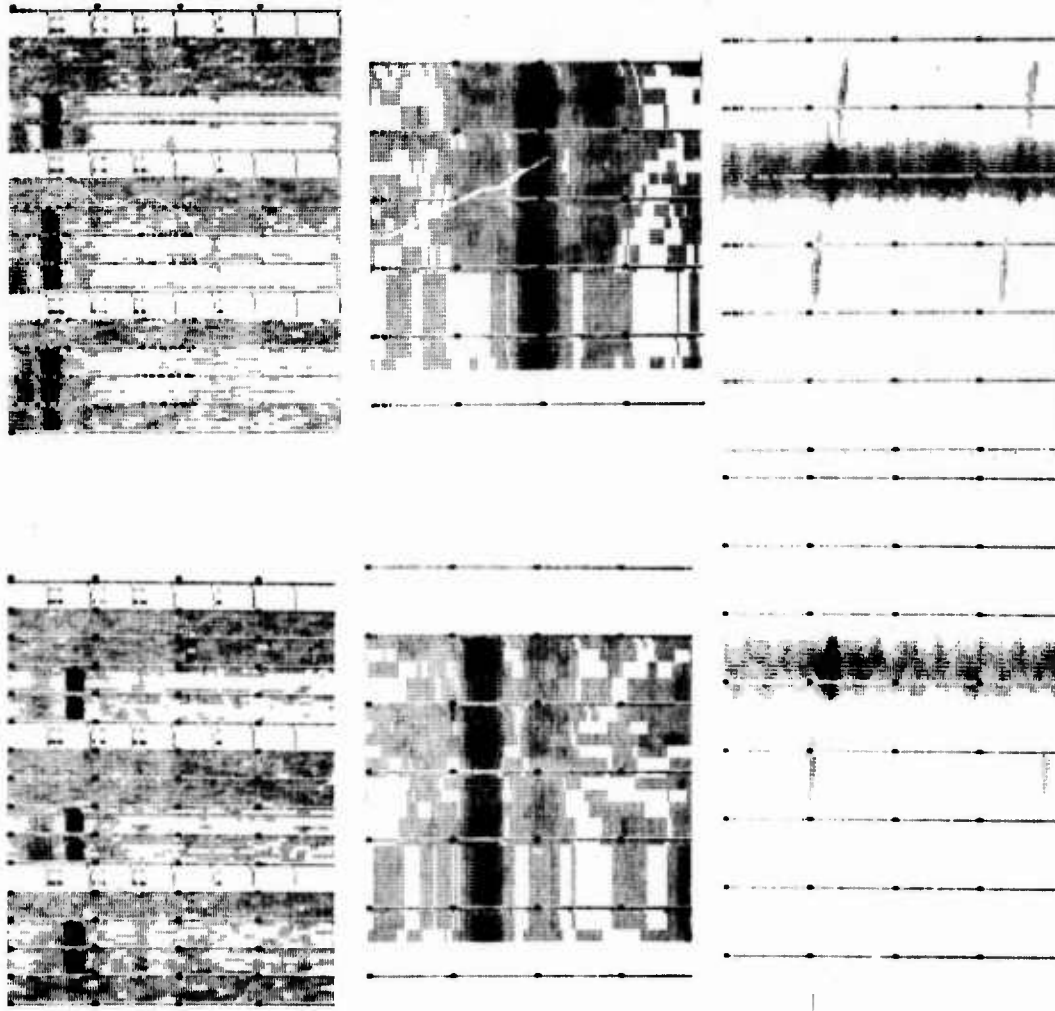


Fig. 11 a b c  
d e f

TABLE 12  
Digicoder Integers  $\leftrightarrow$  Coherence Values

0	$Coh < 0.3095$
1	$0.3095 \leq Coh < 0.5649$
2	$0.5649 \leq Coh < 0.7443$
3	$0.7443 \leq Coh < 0.8565$
4	$0.8565 \leq Coh < 0.9217$
5	$0.9217 \leq Coh < 0.9579$
6	$0.9579 \leq Coh < 0.9776$
7	$0.9776 \leq Coh < 0.9881$
8	$0.9881 \leq Coh < 0.9937$
9	$0.9937 \leq Coh < 0.9967$
10	$0.9967 \leq Coh < 0.9982$
11	$0.9982 \leq Coh < 0.9991$
12	$0.9991 \leq Coh < 0.9995$
13	$0.9995 \leq Coh < 0.9997$
14	$0.9997 \leq Coh < 0.9999$
15	$0.9999 \leq Coh$

REFERENCES

- [1] Capon, J., (et al) Proc IEEE., V.55, p 192-211
- [2] Pfister, W., Sales, G.S., Varad, R., Environmental Research Papers, No. 506, AFCRL-TR-75-0194
- [3] Richards, D.W., Instrumentation Papers, No. 178, AFCRL-72-0475
- [4] Sales, G.S., Varad, R., Videberg, J., Environmental Research Papers, No. 516, AFCRL-TR-75-0290
- [5] Yaglom, A.M., "An Introduction to the Theory of Stationary Random Functions", Englewood Cliffs, N.J., Prentice-Hall Inc., 1962.